國立臺灣大學電機資訊學院光電工程學研究所

碩士論文

Graduate Institute of Photonics and Optoelectronics

College of Electrical Engineering and Computer Science

National Taiwan University

Master's Thesis

利用 940nm 超穎透鏡的瞳孔偵測

Pupil Detection by Using 940nm Metalens

馮博暉

Bo-Huei Fung

指導教授：蘇國棟 博士

Advisor: Guo-Dung J. Su, Ph.D.

中華民國 114 年 01 月

January 2025

doi:10.6342/NTU202404691

國立臺灣大學碩士學位論文
口試委員會審定書
MASTER’S THESIS ACCEPTANCE CERTIFICATE
NATIONAL TAIWAN UNIVERSITY

利用 940nm 超穎透鏡的瞳孔偵測
Pupil Detection by Using 940nm Meta-lens

本論文係馮博暉君（學號 R11941031）在國立臺灣大學光電工程學研究所完成之碩士學位論文，於民國 113 年 11 月 19 日承下列考試委員審查通過及口試及格，特此證明

The undersigned, appointed by the Graduate Institute of Photonics and Optoelectronics, on 19 November 2024 have examined a Master’s thesis entitled above presented by FUNG-BO-HUEI (student ID: R11941031) candidate and hereby certify that it is worthy of acceptance.

口試委員 Oral examination committee:

（指導教授 Advisor）

蘇國棟　　林建中　　丁建均

所長 Director: 吳育任

誌謝

碩士生涯稍縱即逝，轉眼間，畢業的時刻已悄然而至，回首過往，我受過許多貴人的幫助，而指導教授蘇國棟老師就如同引路人，在我徬徨的時候，給我指導，無怨無悔的悉心教導我，也感謝在數據整理的過程中，給予我指導建議的丁建均教授，讓我能夠平順的完成論文。

在求知過程，我遇到許多的困難，感謝同學們的協助，才讓我有勇氣能夠走完這趟旅程，不管是負責製程的學長姐(晉笠、珮瑜)，給予我製程方面的建議，亦或是一起合作量測的學長(聖輝)，給予我量測上的一些經驗以及叮嚀，甚至是負責模擬的同學(宇翔和寬程)，所提供我關於光學模擬的知識，還有即使研究領域不同，仍然給予我支持的同學(昱萱、又方、靖詠和元凱)，以及不同實驗室，但卻能夠彼此交流製程經驗的學長(電子所的伯叡學長)， 有你們的幫忙才成就現在的我，也謝謝你們旅途上的陪伴，也祝福未來的你們，在各個領域皆能大放異彩。

隨著我在實驗室的旅途即將畫下句點，希望學弟妹們(顗瑄、昀翰、嫚婷、際龍、佑蓁、瑞明、崇安)，能夠接替將實驗室延續下去，也預祝你們實驗順利，特別是製程組的學弟妹(顗瑄和昀翰)。

最後，感謝我的父母以及家人，無條件支持我，給予我一些關於待人處事的建議和人生的規劃，以及身邊的朋友，在我不順遂的時候，給予我重新出發的動力。雖然一路上充滿挑戰，但都我始終朝著目標前行，期許未來自己能夠做出貢獻。

中文摘要

為了運用光的物理性質，傳統透鏡往往需要多種透鏡組合而成，因此受限於鏡片厚重的困擾，而超穎透鏡則可以解決此困境。

它是利用電腦進行計算及模擬，結合半導體製程技術，製作出一種具有次波長尺寸的微型結構，其本身非常微小，在現有的材料上進行表面的加工，透過產生特定線寬的奈米柱排列，以改變入射光的物理性質，進而達成聚焦的效果來偵測瞳孔。

在我本篇論文中，運用製程技術將非晶矽作為超穎透鏡的材料製作於玻璃基板上。首先我使用電子束光刻(正光阻)將圖案呈現在材料上，畫出所需奈米結構的圖案，緊接著蒸鍍一層鎳金屬作為蝕刻的遮擋層，再經過 lift-off 的步驟去除光阻與其上方金屬，並保留圖案，最後再使用，感應耦合式的電漿離子蝕刻出非晶矽的奈米柱。

我將製作於透明基板上的超穎透鏡結合現有的光學感測元件，將瞳孔的影像透過超穎透鏡聚焦於光學感光元件上，並利用公開平台上的瞳孔偵測軟體，進行瞳孔偵測，為超穎透鏡應用於瞳孔偵測取得了階段性的成功，未來期待能將成果運用於更多領域上。

關鍵字：超穎透鏡、非晶矽、電子束顯影、光學量測

doi:10.6342/NTU202404691

ABSTRACT

To regulate the physical properties of light, traditional lenses often require a combination of multiple lenses, resulting in bulkiness. However, metalens can overcome the limitations of conventional lenses.

They are created using computational capabilities and software for optical simulations, and finally fabricated with semiconductor processing techniques. These metalens are composed of sub-wavelength-sized microstructures. By fabricating specific patterns of nanostructures on the surface of existing materials, they can manipulate the physical properties of light, and achieve focusing effects, such as for pupil detection.

In this thesis, semiconductor fabrication techniques are employed to create metalenses consisting of amorphous silicon on a transparent glass substrate. First, I employed electron-beam lithography (positive resist) to define the necessary nanostructures on the material. Then, a thin layer of metal (nickel) was deposited as an etching protection layer, After the lift-off process, the resist and the metal will be removed, leaving only the pattern standing. Finally, inductively coupled plasma reactive ion etching (ICP-RIE) was used to etch.

doi:10.6342/NTU202404691

I fabricated metalens on transparent substrate and integrated it with existing optical sensing components, focusing the pupil's image onto the optical sensor through the metalens. Using open-source pupil detection software, I successfully detected the pupil, achieving a milestone in applying metalenses for pupil detection. In the future, I look forward to extending these results to other fields and applications.

Keywords: metasurface, subwavelength interface, amorphous silicon, electron-beam lithography, optical measurement

CONTENTS

doi:10.6342/NTU202404691

doi:10.6342/NTU202404691

doi:10.6342/NTU202404691

FIGURES LIST

doi:10.6342/NTU202404691

doi:10.6342/NTU202404691

doi:10.6342/NTU202404691

doi:10.6342/NTU202404691

TABLES LIST

doi:10.6342/NTU202404691

Chapter 1 Introduction

Pupil detection has become increasingly common in various fields, including optics and healthcare. In this thesis, we utilize a 940nm LED and a metalens with an optical sensor (CMOS) to create a compact infrared camera. By miniaturizing the camera, it offers a lightweight new model that can be used in future applications where compact devices and instruments are needed across different industries.

1.1 Principle of Metalens

With the rapid development of metasurface technology, its application in lenses has gradually increased. Compared to bulky traditional lenses, metalenses have the advantages of being compact and lightweight. They are composed of multiple nanostructures (nanopillars), making them more suitable for ultra-thin micro-optical applications.

Metalens is mainly divided into three components: metasurfaces, metamaterials, and meta-interfaces [1]. By adjusting the composition of these three components, the behavior of light can be precisely controlled. First, the metasurface, composed of numerous nanostructures (nanopillars), forms a subwavelength-scale structure at the interface, enabling effective manipulation of light's physical properties, including

doi:10.6342/NTU202404691

polarization, phase, amplitude, and dispersion. Second, the periodic arrangement of the structure is determined by metamaterials, which influence light behavior through collective resonance. Finally, the meta-interface highlights the "two-dimensional distribution" and "independence" of the system, utilizing the near-field phase and amplitude produced by the nanostructures to manage light in the far field, thus overcoming the limitations of conventional diffraction devices.

A metalens is a unique form of metasurface that possesses both focusing and imaging capabilities, enabling it adjust the wavefront and the phase of light. Based on Huygens-Fresnel principle, each point on a light wavefront acts as a point source, radiating secondary waves [2]. The combined envelope of these secondary waves forms the propagated wavefront. By utilizing a radial arrangement of nanopillars, metalens can manipulate key physical properties of light, including phase, polarization, amplitude, allowing it to shape the optical wavefront into any desired subwavelength resolution [3].

When light transitions between two media with different refractive indices, secondary waves are produced at the interface regarding to the shift in refractive index. The process is described by Snell's law, which governs how light is refracted at the boundary between the two media.

doi:10.6342/NTU202404691

Snell's law:

$$\frac{\sin\theta_2}{\sin\theta_1}=\frac{v_2}{v_1}=\frac{n_2}{n_1} \quad (1.1.1)$$

Traditional lenses operate based on Snell's law, which explains how light is refracted and propagates as it moves between different media. According to Snell's law, θ1 is incident angle, while θ2 is reflection angle. The refractive indices of two media are represented by n1 and n2, and the propagation velocities of light in these media are denoted as v1 and v2. When light travels through media with differing refractive indices, the variation in incident angles causes refraction, while differences in propagation speed lead to an optical path difference. Metasurfaces address the issue of light deviation from refraction by modifying the light's phase and wavefront.

Furthermore, different wavelengths of light are refracted at different angles, causing dispersion. Traditional lenses are unable to focus multiple wavelengths onto the same plane, leading to chromatic aberration [4-6]. In contrast, metalenses are not limited by the curvature of the lens surface. By employing various nanopillar arrays, they can control the direction of light refraction and its propagation properties. With careful design, metalenses can introduce specific phase shifts for different wavelengths of light, allowing for adjustments in focal length or focusing behavior across wavelengths, effectively managing both dispersion and chromatic aberration.

doi:10.6342/NTU202404691

1.2 Metalens Design and Simulation

Several crucial factors must be taken into account when designing metalenses, including the structure’s shape, phase modulation, wavelength range, and choice of materials. By utilizing small pillar-shaped or circular structures on the metasurface, the size of these elements can dictate the focusing capability and wavelength selectivity of the metalens. Additionally, the arrangement of these structures performs a crucial point to determining optical imaging resolution which can influence the degree of dispersion.

By adjusting the height, thickness, or refractive index of the nanostructures, phase modulation in metalenses can be controlled, enabling precise control over the phase. These parameters can be fine-tuned to manipulate the phase profile of incident light, allowing for customized focusing and wavefront shaping. In addition, the choice of materials is vital, as it defines the optical properties—such as refractive index and dispersion—that significantly influence the performance of the metalens, especially in terms of focusing accuracy and aberration correction [7, 8].

In contrast to traditional lenses that focus light through gradual phase accumulation within refractive materials, metalenses achieve focusing by implementing abrupt phase modulation across subwavelength meta-units.

doi:10.6342/NTU202404691

To design a metalens that operates similarly to a spherical lens, hyperbolic phase profiles can be modeled based on the optical phase difference [9], as described below.

$$\varphi(x, y) = -\frac{2\pi}{\lambda_0}\left(\sqrt{x^2 + y^2 + f^2} - f\right) \tag{1.2.1}$$

Here, λ_0 represents the incident wavelength in free space, and f denotes the focal length. For AR utilization, phase-modulating meta-surfaces are widely used for various wavefront engineering tasks. Different configurations of meta-units can create phase modulation mechanisms that are suitable for specific conditions [10]. To optimize efficiency in this system, we employ a propagation-type metalens to make the most of the non-polarized emission from the LED. The metalens features a numerical aperture (NA) of 0.15, and a diameter of 1.5 mm, and a focal length of 5 mm, corresponding to a f/# of 3.33.

Previous studies have shown that ZEMAX optical software can model diffractive optical elements and optimize the desired phase profiles for metalenses using ray tracing techniques [11,12]. The metalens phase profile is described as follows.

$$\varphi_{metalens} = \mathrm{M}\sum_{i=1}^{N} A_i E_i(x, y) \tag{1.2.2}$$

M represents the diffraction order, the number of polynomial terms is N, the coefficient for each extended polynomial term used to optimize the smallest root mean

doi:10.6342/NTU202404691

square (RMS) spot size through the damped least-squares method is Ai, and Ei (x, y) indicates the phase distribution, expressed as a polynomial expansion in the spatial coordinates x and y. Using this equation, the ideal phase profile for the target metalens can be calculated and simulated with ZEMAX software. Fig. 1-1 presents the ideal target phase distribution of the designed metalens, displaying a symmetric concentric circular contour that signifies a 2π phase shift variation on the subwavelength structures.

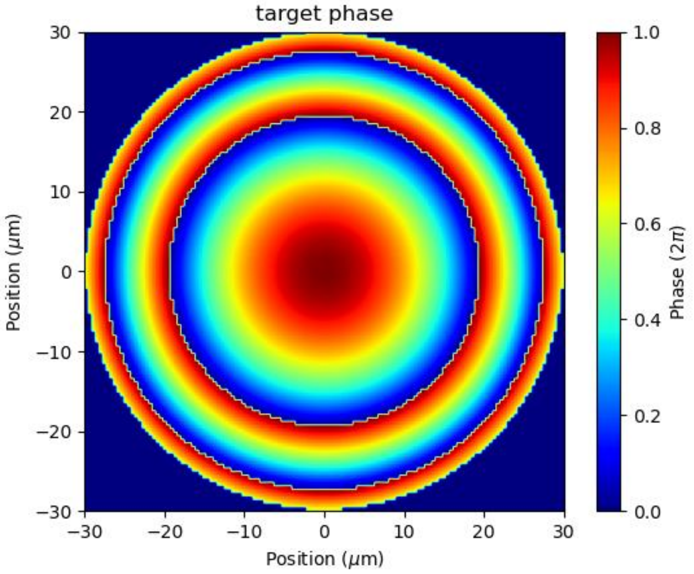

Fig. 1-1 The ideal target phase profiles

In this configuration, each dielectric meta-atom acts as a dielectric waveguide, truncated to exhibit low reflectivity at both top and bottom interfaces. The desired phase-shift modulations are obtained by modifying the parameters of the meta-units, including height, cross-sectional dimensions, lattice spacing, and effective refractive index. Given the use of a 940nm wavelength light source, a-Si was selected as the

doi:10.6342/NTU202404691

material for the metalens due to its high transmittance in the near-infrared spectrum at a wavelength of 940 nm. To ensure manufacturability, the effect of fabrication accuracy on performance is considered. As a result, a compromise is made by selecting square nanopillars, which offer a symmetric structure suitable for near-eye displays without specific polarization requirements. A structural phase library is then developed, linking the phase shift and transmittance of the meta-units to their geometric parameters—span, pitch, and height—using the S-parameter extraction method in finite-difference time-domain (FDTD) simulations performed using Lumerical Inc. software. Optimized nanostructures with high transmittance are selected to achieve a complete 0 to 2π phase shift range, ensuring high efficiency. These square columnar structures feature a height of 570 nm, a pitch of approximately 260 nm, and a span varying between 50 nm and 250 nm. Notably, the phase shift of 2π is realized by modifying cross-sectional dimensions of nanopillars within range of 50 nm to 250 nm, with all these structures demonstrating excellent transmittance.

The metalens is constructed by integrating the phase accumulation library with the meta-unit dimensions and the desired phase profile. To verify the performance of metalens, numerical simulations are conducted using the FDTD method with a plane wave at a wavelength of 940 nm. A near-field to far-field transformation [13] is applied to capture the intensity distribution at the focal plane. Due to the substantial

doi:10.6342/NTU202404691

computational demands of a metalens with a 1500 µm diameter, the analysis is concentrated on the x-z plane, as shown in Fig. 1-2.

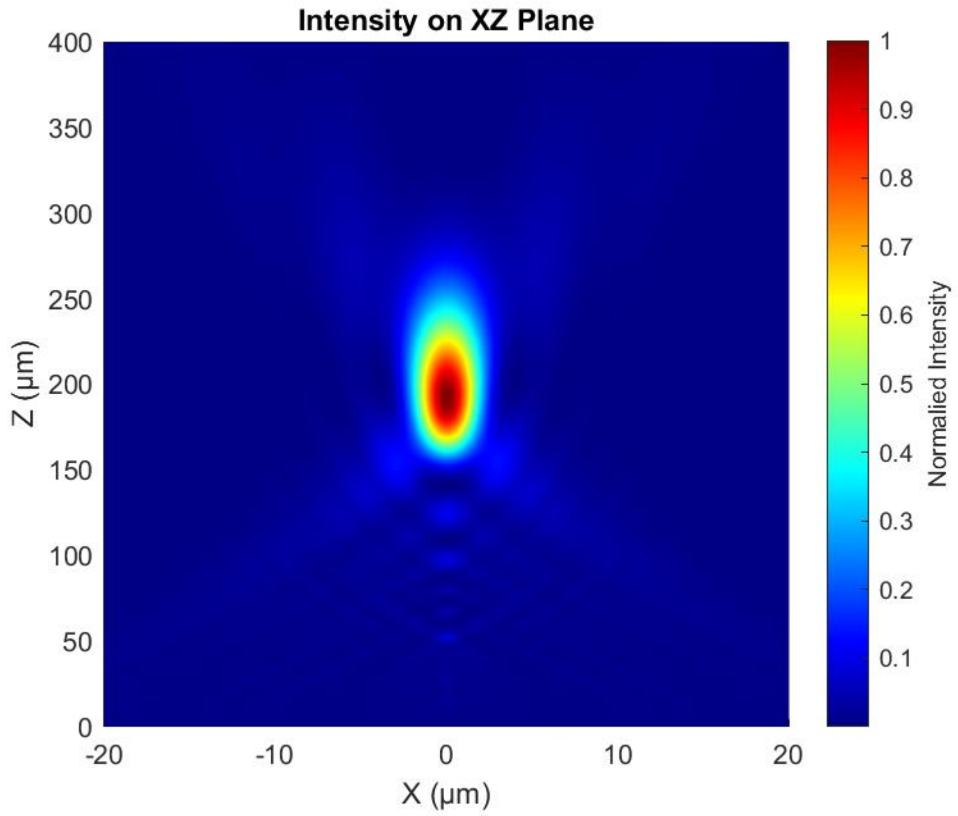

Fig. 1-2 Intensity distribution of a 1500 μm diameter metalens on the x-z plane.

The simulated focusing position and performance closely match our design specifications, confirming the achievement of a 5 mm focal length for the focusing metalens. To further analyze the characteristics of this metalens, a scaled-down version with a diameter of 60 µm was designed. This scaled metalens uses the same NA value and meta-unit parameters as the original and is subjected to identical simulation procedures. The reduced size eliminates computational constraints, enabling comprehensive data collection and detailed characterization.

Fig. 1-3 illustrates the electric field intensity distribution in the x-y plane. The focusing efficiency is calculated to be 67.5%, determined by integrating the focal plane intensity within a spot size equal to three times the radius of the Airy disk's full width at half peak (FWHM) and dividing it by the total intensity of the light source [14].

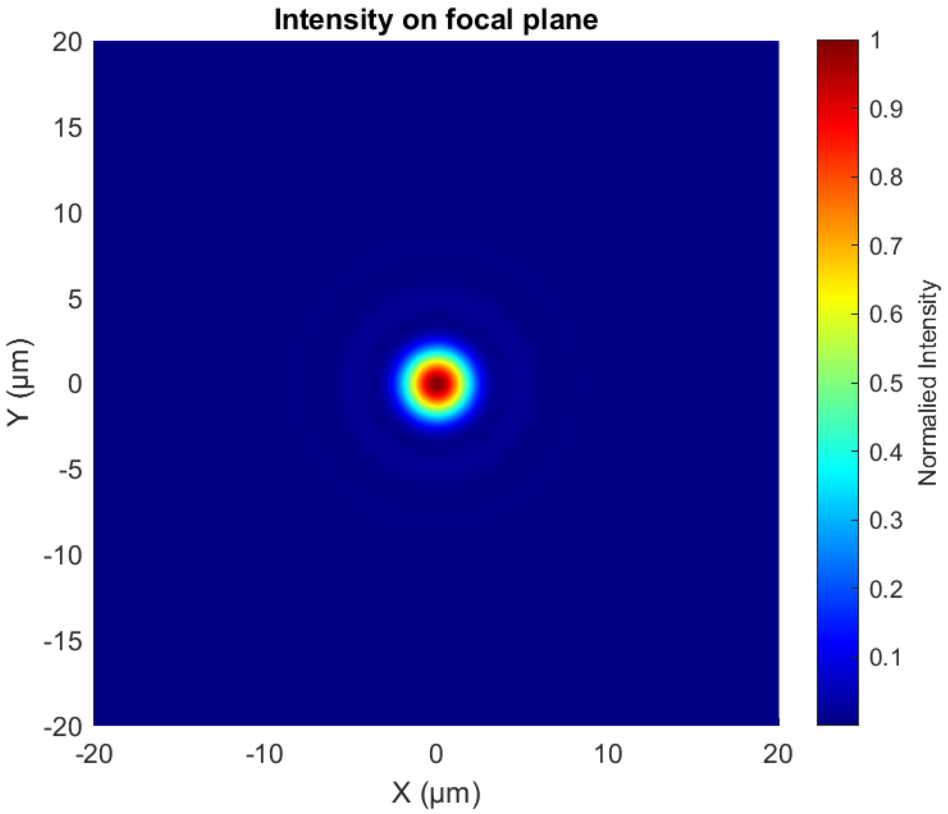

Fig. 1-3 Intensity distribution of a 60 μm-diameter metalens on the x-y plane.

Furthermore, the optical performance is assessed by comparing the intensity pattern to theoretical values. The Airy disk pattern intensity follows the Fraunhofer

doi:10.6342/NTU202404691

diffraction equation for a circular aperture, which is represented by the squared modulus of the aperture's Fourier transform, given by:

$$I(\theta) = I_0 \left[\frac{2J_1(kasin\theta)^2}{kasin\theta}\right]^2 \qquad (1.2.3)$$

Here, I(θ) denotes diffraction intensity at a point in the observation plane, I_0 is maximum intensity at center of Airy disk, J_1 represents the first-order Bessel function, k is wavenumber, a is aperture radius, and θ is incident angle.

This scaled-down version serves as a reference for the 1500 μm-diameter metalens, allowing us to estimate the efficiency and confirm that the metalens designed through these simulation steps exhibits performance characteristics consistent with theoretical predictions.

In this thesis, we demonstrate the integration of metalens with 940nm LED and CMOS camera for pupil detection. A simple schematic is shown in Fig. 1-4 (a). Metalens we designed consist of square nanopillars with a height (h) of 570 nm and side widths (w) varying from 50 to 250 nm, as illustrated in Fig. 1-4 (b) and (c). By varying the nanopillar widths, the structural parameters are modified to accomplish the necessary phase coverage of 0–2π, forming a circular metalens, as illustrated in Fig. 1-4 (d).

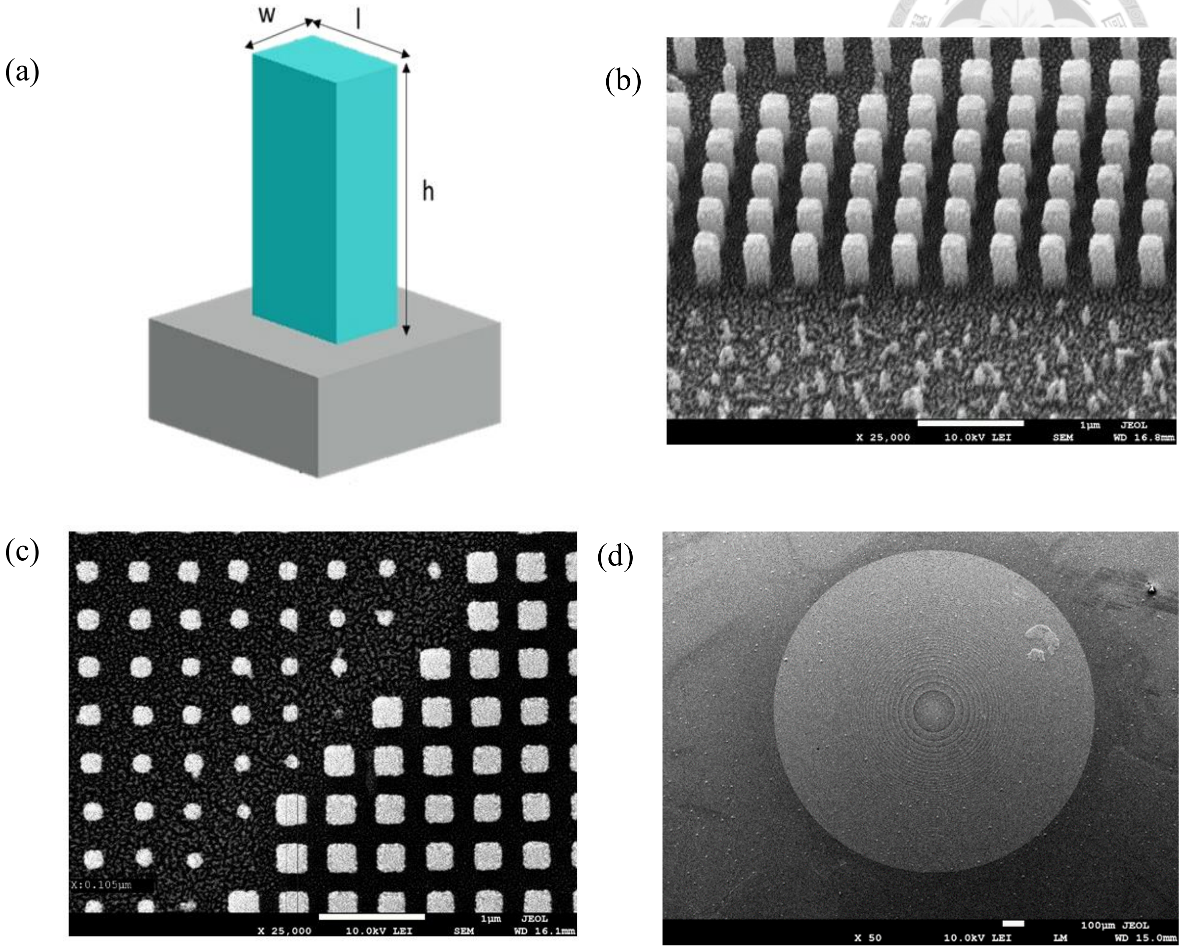

Fig. 1-4 (a) A schematic of square nanopillars for a metalens. (b) SEM image of square nanopillars with a height of 570 nm. (c) SEM image of square nanopillars with side widths ranging from 50 to 250 nm. (d) SEM image of a circular metalens with 1500 µm diameter.

Each nanopillar unit operates independently, with its neighboring structures having no influence on the light passing through the unit. Simulations using near infrared light with a wavelength of 940 nm demonstrate that metalenses with varying nanopillar sizes can produce different refraction and focusing effects. The measured focusing efficiency is around 61.4%.

The goal of fabricating large-area metalens is to enable practical applications of this technology in pupil detection. By integrating 940nm LED with metalens, we enhance the control of light, focusing it precisely on the CMOS camera. This enables developers to accurately detect the user's eyes, particularly the pupils, which helps ensure that images are presented clearly in front of the user.

This integration opens up exciting possibilities for various applications, including wearable displays, high-resolution displays, optical communication, and sensing systems. Ultimately, combining 940nm LED with large-area focusing metalens brings metalens technology closer to real-world applications and expands its potential across a range of optical devices and systems.

doi:10.6342/NTU202404691

1.3 Eye Tracking

The applications of eye tracking are extremely diverse, spanning multiple fields, from entertainment to healthcare and human-computer interaction. Eye tracking technology can be found across all these areas. Here, I have outlined six of the more common applications: Medical Diagnostics, Psychology and Market Research, Virtual and Augmented Reality (VR/AR), Autonomous Driving and Driver Monitoring, Education and Training, Human-Computer Interaction.

Among these, VR and AR have specific requirements for cameras. They often necessitate the use of wearable devices, such as AR/VR glasses, to achieve immersive virtual and augmented reality experiences, thus requiring miniature cameras. Metalenses, composed of meta-optics, offer several advantages in this context, including: Space efficiency, Weight reduction, Lower power consumption, Low latency and high refresh rates, Cost control, Easy integration with infrared light sources.

Therefore, miniature cameras for AR/VR eye tracking applications can meet demands in terms of space, weight, power efficiency, and responsiveness, while also balancing cost and comfort, making them an ideal solution.

There are currently many methods used for eye tracking, with six commonly seen techniques: Corneal Reflection, Pupil Tracking, Electrophysiological Recording,

doi:10.6342/NTU202404691

Electroencephalogram, Video Recording, and Laser Scanning. Table 1-1 [15] presents pros and cons of these six methods.

Methods	Optical		Electrophysiological		Computer Vision and Image Processing	
	Corneal Reflection	Pupil Tracking	Electrophysiological Recording	Electroencephalogram	Video Recording	Laser Scanning
Accuracy	high	high	medium	low	high	high
Precision	high	relatively high	medium	low	high	extremely high
Equipment Portability	high	high	low	low	medium	low
Cost	high	high	high	high	medium	high
Sensitivity to Environmental	high	medium	low	high	high	low
Delay	low	low	extremely low	medium	medium	low

Table 1-1 Parameters of eye tracking methods [15].

doi:10.6342/NTU202404691

Electrophysiological Recording, Electroencephalogram, and Laser Scanning all have drawbacks, such as complex equipment and uncomfortable wearing experience. Video Recording, meanwhile, has high resolution requirements and high power consumption. As a result, these four methods are not suitable for use in medical instruments or wearable devices (AR/VR glasses).

In contrast, Pupil Tracking and Corneal Reflection offer high accuracy, suitability for dynamic environments, low latency, and high real-time performance. However, compared to Corneal Reflection, Pupil Tracking is more cost-effective, requires simpler calibration, and is less sensitive to external lighting and head movement. Therefore, Pupil Tracking is better suited for medical instruments or wearable devices (AR/VR glasses) than Corneal Reflection.

1.4 Comparing LED and Laser

In optical measurements, the most commonly used light sources are LEDs and lasers. Lasers concentrate energy in a specific area, resulting in very high power density, and if the emission power is too high, they can easily cause harm to the human body. Compared to lasers, LEDs have a lower power density, so selecting an LED with a low emission power (less than 1mW/cm^2) for measurements is safer. Even when directly exposed to the human body, including the eyes, the risks are significantly lower than with lasers [16].

Therefore, using LEDs as a light source can enhance measurement safety (the beam width of an LED is typically 10 times that of a laser, meaning the power density of an LED is about 1/100th of that of a laser). A comparative illustration of the power density between LED and laser is shown in Fig. 1-2. In this thesis, we have chosen to use LEDs with an emission power of less than 1mW to prevent any harm to the human eye during measurements.

doi:10.6342/NTU202404691

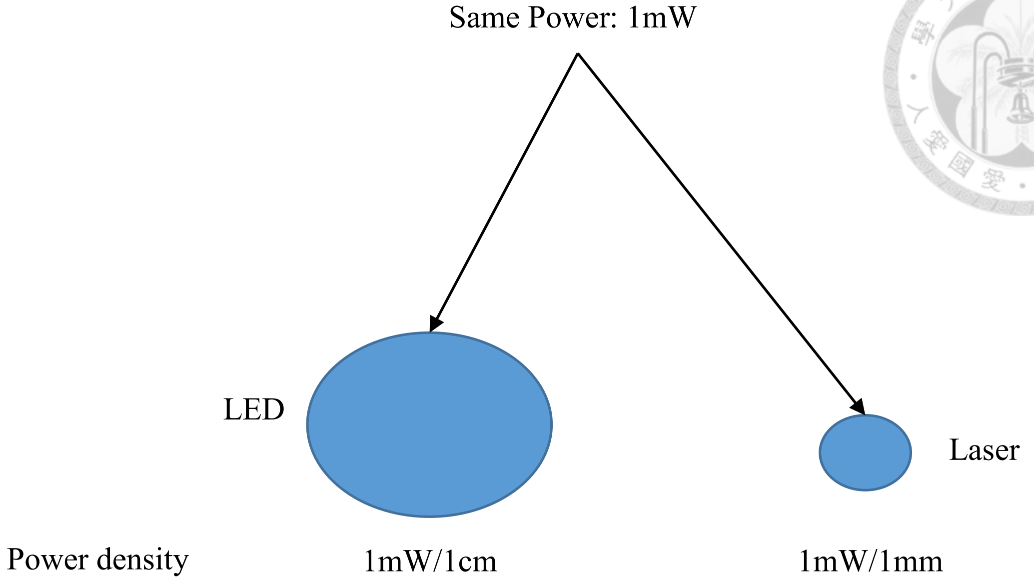

Fig. 1-5 the power density between LED and laser

doi:10.6342/NTU202404691

1.5 Comparison between 940 nm LED and 850 nm LED.

The most common near-infrared LEDs on the market are 940 nm and 850 nm. The 850 nm LED emits a faint red glow, as it is close to the visible red light spectrum (around 720 nm). If the observer is sensitive to infrared light (capable of seeing slight near-infrared light in the 720–820 nm range), prolonged observation may cause dizziness, nausea, or other symptoms (a phenomenon known as "red glow effect"). In contrast, the 940 nm LED, being further from the visible spectrum, emits almost no red glow when illuminated, thus avoiding the red glow effect during observation.

Additionally, the 940 nm LED is more tolerant to noise and offers easier detection. making it a more suitable choice as a light source for pupil detection. A comparison table of the 850 nm and 940 nm LEDs is shown in Table 1-2 [17].

Item	850 nm high power	940 nm on the market	940 nm newly developed
Output power	5 mW ○	2 mW △	5 mW ○
Invisibility	×	○	○
Tolerance	×	○	○
Scattering	△	○	○
Frequency response	△	×	○

Table 1-2 The comparison between 850 nm and 940 nm LEDs [17]

1.6 Infrared Camera

An infrared imaging camera is a device that records images using infrared (IR) light, which cannot be seen by the human eye but can reveal unique details and perspectives. In infrared photography, the camera detects wavelengths of light beyond the visible spectrum, typically from around 700nm to 1000nm. This type of photography produces distinctive images where foliage appears bright white, skies can turn dark, and certain materials reflect light in unexpected ways.

The infrared camera has several advantages in pupil detection, such as independence from lighting conditions, high sensitivity, reduced reflection issues, non-contact detection and so on [18].

In summary, infrared camera offers numerous advantages in pupil detection, making it an ideal choice for many applications.

doi:10.6342/NTU202404691

1.7 Motivation

In today's life, cameras have become an indispensable part of our daily experiences, whether in smartphones, computers, wearable interactive devices, or medical instruments. However, traditional cameras are usually composed of lens assemblies, often requiring bulky conventional lenses to overcome aberration and chromatic distortion issues. To address these challenges, research on metalenses has been steadily increasing. With the latest developments in metalens technology, through the arrangement of different nanostructures, metalenses are able to overcome the limitations of traditional lenses, featuring greater lightweight and miniaturization, allowing for more diverse applications of cameras.

Thanks to the efforts of senior researchers in the laboratory, significant progress has been made in the fabrication of electrically controlled tunable focusing metalenses [19]. This thesis aims to utilize the thin and lightweight characteristics of metalenses, along with their focusing abilities, for pupil detection, combining image processing and artificial intelligence for simple analysis, in preparation for larger-scale practical applications of pupil detection.

Chapter 2 Fabrication Technology

The fabrication of metalens is closely related to image quality. If there is a huge deviation between the fabricated lens and the design, the image quality will also be affected. Therefore, successfully manufacturing the metalens is the first step for the experiment to succeed.

In the future, as semiconductor manufacturing technology advances, lenses can be made larger while the critical dimension becomes smaller, leading to improved image quality. If the manufacturing process becomes mature and stable, the application of metalens in pupil detection will also be expanded.

2.1 Cleaning

For glass substrates, cleaning is a crucial step that directly impacts the quality of the subsequent epitaxial a-Si layer. Proper cleaning increases the surface flatness and uniformity of the wafer, preventing localized differences during the later fabrication of metalens. The cleaning process involves the following four steps:

1. Place the glass substrate in an acetone solution and use ultrasonic vibration for 3 minutes to remove surface organic materials.

doi:10.6342/NTU202404691

2. Place the glass substrate in a methanol solution and use ultrasonic vibration for 2 minutes to remove any residual acetone.
3. Place the glass substrate in deionized water and use ultrasonic vibration for 2 minutes to remove surface ions and residual impurities.
4. Use a nitrogen air gun to dry the glass substrate, then place it on hot plate and set to 130°C and bake for 1 minute, ensuring any remaining deionized water is evaporated. Hot plate is depicted in Fig. 2-1 below.

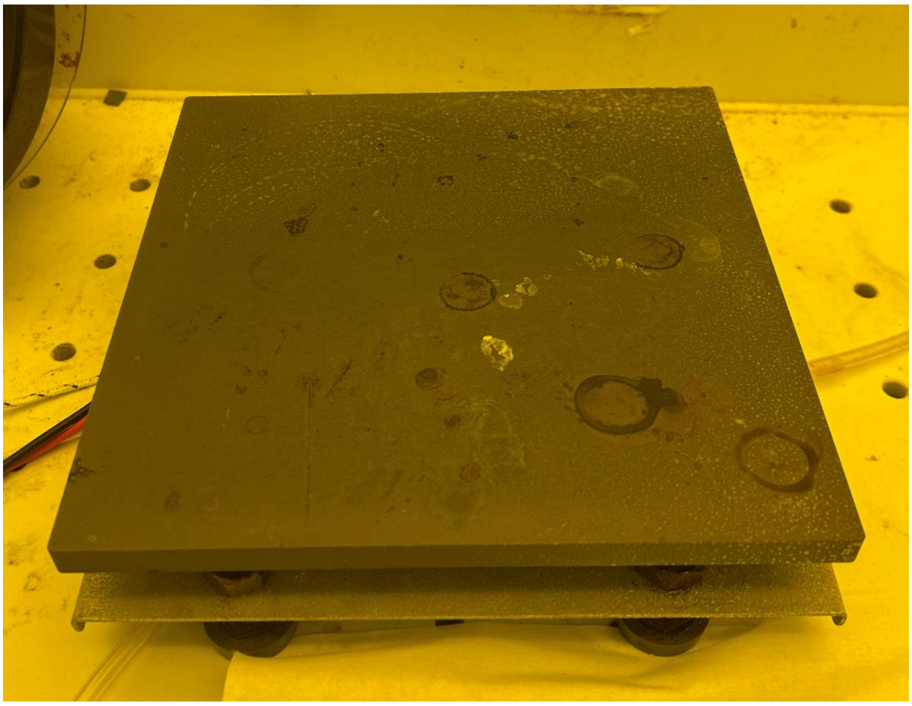

Fig. 2-1 Hot plate.

doi:10.6342/NTU202404691

2.2 Lithography

In semiconductor manufacturing, the photolithography process is a critical step that determines success or failure. It involves using a photoresist to transfer the designer's pattern onto a wafer. Even slight defects in the photolithography process can result in incomplete pattern transfer, leading to missing or distorted patterns. This, in turn, may cause the fabricated wafers to experience reduced efficiency or functionality.

2.2.1 Lithography step

The steps of the lithography are shown in Fig. 2-2 and consist of seven steps in total:

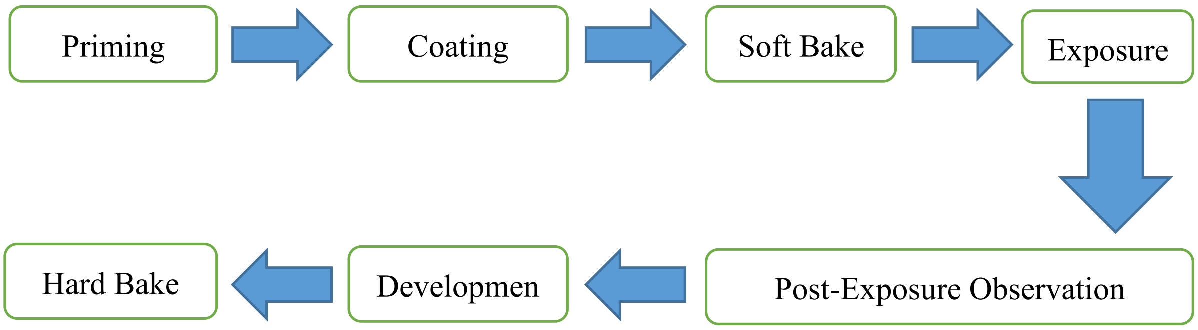

Fig. 2-2 Flow chart of lithography process

1. Priming

   The sample is placed on a chuck in the spin coater, and hexamethyldisilazane (HMDS) is applied to the surface. HMDS enhances the adhesion of the photoresist to the sample, increasing the stability of the sample during the photolithography process.

2. Coating

   The sample is placed on a spin coater, and photoresist is applied to the surface. Since the photoresist is more viscous than HMDS, a higher spin speed is needed to achieve uniform coverage.

3. Soft Bake (Pre-exposure Bake)

   This step ensures that the moisture and solvents in the photoresist are evaporated and the photoresist is solidified, enhancing its adhesion to the sample surface.

4. Exposure

   This step is the most important step in the entire photolithography process. The photoactive compounds in the photoresist undergo a photochemical reaction depending on the specific wavelength of the exposure light source. In positive photoresist, exposure to light breaks the polymer chains, while in negative photoresist, exposure causes solidification. Therefore, the choice of photoresist results in different pattern outcomes.

In this thesis, we use electron-beam lithography (EBL) for exposure. Electrons, with their extremely short wavelength, allow for nanoscale precision, making EBL an invaluable tool for creating the critical dimension at the nanometer scale. However, EBL has a significant drawback: unlike stepper or scanner exposure tools, which expose an entire surface at once, EBL exposes the sample point by point using the electron beam. As a result, the process is time-consuming, which is one of its main limitations.

5. Post-Exposure Observation

   After exposure, a basic observation is performed using an electron microscope to confirm that the pattern matches the blueprint provided in the design. The inspection checks for any exposure defects, such as pattern deformation, missing areas, or misalignment of the pattern.

6. Development

   The developer solution is applied to the surface of the sample, ensuring that the exposed areas are fully covered by the solution. It is a relatively gentle developer, reducing the risk of erosion in unexposed areas and offering a broader process window.

doi:10.6342/NTU202404691

After development, the pattern is solidified. If post-exposure observation shows that the pattern does not match the expectation, the sample can be immersed in an acetone solution to remove the photoresist and reapply a fresh layer for a new exposure. However, once the pattern is solidified after development, acetone cannot easily remove the photoresist for re-exposure.

7. Hard Bake

The sample is placed on a hot plate for hard baking at a temperature of 130℃ for 1 minute to ensure that any remaining solvents on the surface are evaporated. This process also increases the hardness of the photoresist, helping to maintain the stability of the pattern.

doi:10.6342/NTU202404691

2.2.2 Electron-Beam Lithography

EBL is the most commonly used tool in semiconductor processing for exposing nanoscale or microscale patterns.

In this thesis, we used the ELS-7800 as the EBL instrument, as shown in Fig. 2-3.

Fig. 2-3 Electron-beam Lithography (Elionix, ELS-7800).

doi:10.6342/NTU202404691

It operates based on the principles of a scanning electron microscope, allowing pattern definition without the need for any masks. As the wavelength of electrons is much smaller compared to that of light used in traditional exposure machines, the focused electron beam can precisely and accurately strike the uniformly coated photoresist on the sample, achieving higher resolution and creating smaller line-width structures [20].

During EBL exposure, the positive photoresist undergoes a photochemical reaction when irradiated by the electron beam, causing the polymer chains to break and resulting in a difference between the exposed and non-exposed areas. Increasing this difference is crucial for creating high-resolution patterns. Additionally, various parameters related to the electron-beam equipment—such as electron dose, sample size, pixel size (dotmap), exposure time, as well as environmental factors like humidity and temperature—affect the quality of the lithography process.

When the electron dose is too high, the positive photoresist is overexposed, causing the exposure line width to decrease, leading to pattern distortion or even loss. Conversely, when the dose is too low, the positive photoresist is underexposed, causing the line width to increase, making it difficult to accurately expose small line-width

doi:10.6342/NTU202404691

patterns. Both situations affect the subsequent imaging quality, making precise dose control essential.

The choice of pixel size can be determined based on the minimum line-width requirements of the design. Finer pixels provide higher resolution, but at the cost of longer exposure times [21].

Additionally, the electron beam current required for exposure can be measured by aligning the Faraday cup using the scanning electron microscope on the machine. The exposure time is correlated with the current and the previously mentioned dose. Inaccurate measurements can lead to overexposure or underexposure issues, which can have irreparable consequences during the lift-off process.

The exposure time can be calculated using the following formula:

$$\mathrm{Time\ (sec)} = \mathrm{Dose}\left({}^{\mu C}\!/_{cm^2} \right) * {}^{\mathrm{Area}\ (\mu m^2)}\Big/_{\mathrm{Current}\ (pA)} \qquad (2.2.2.1)$$

doi:10.6342/NTU202404691

2.3 Lift-off Process

In semiconductor processing, a thin metal layer is commonly applied as a protective shield. For most metals, it offers high corrosion resistance and strong resistance to ion bombardment, making it ideal as a protective mask for etching. However, to match the exposed pattern, a lift-off process is required to create the desired pattern mask.

The flowchart of the lift-off technique is shown in Fig. 2-4.

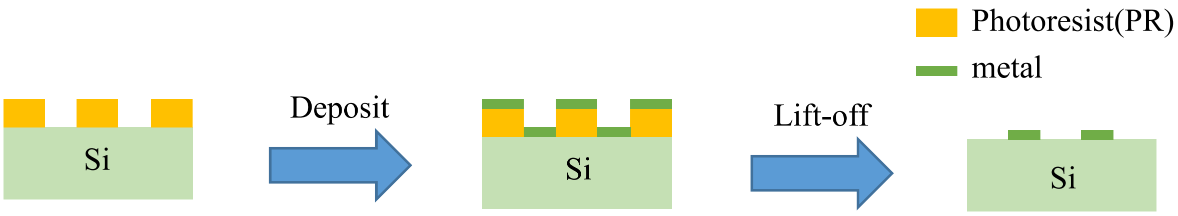

Fig. 2-4 The flowchart of the lift-off process.

First, a thin metal layer is deposited onto the sample after it has been exposed. Then, sample is immersed in a solution, which dissolves photoresist. This allows the metal deposited on the photoresist to float on the surface of the solution, effectively removing the metal from the photoresist. The pattern on the photoresist is then transferred onto the metal in reverse, completing the lift-off process.

doi:10.6342/NTU202404691

Since the pattern resulting from the lift-off process is the inverse of the exposed pattern, the pattern is designed to be the reverse of the intended final design during exposure. This ensures that, after the lift-off process, the pattern is reversed to align with the intended design.

doi:10.6342/NTU202404691

2.4 Etching

In the fabrication process of metalens, etching is the final step, and the quality of etching directly affects quality of nanopillars. Therefore, etching method, time, and materials used for etching all influence the outcome. Etching methods can be categorized into dry etching and wet etching based on the approach used.

2.4.1 Physical Etching

Dry etching implicates bombarding the material’s surface with high-energy ions, causing depressions on surface. Since dry etching is a physical bombardment with high-energy particles, only the areas that are bombarded are etched, while the areas without bombarded remain unaffected. This gives dry etching anisotropic and non-selective properties, making it effective for fabricating nanopillars with high aspect ratios.

2.4.2 Chemical Etching

Wet etching, by contrast, using a chemical solution to react with the material’s surface, creating gaps. Because wet etching relies on the chemical dissolution of the material by the solution, only the materials that chemically react with the solution will dissolve. This gives wet etching isotropic and selective properties, making it effective for removing protective layers and other impurities left behind after dry etching.

The contrast between isotropic and anisotropic etching as shown in Fig. 2-5.

Fig. 2-5 Contrast between isotropic (left) and anisotropic (right)

doi:10.6342/NTU202404691

Chapter 3 Method of Experiment

In this chapter, we will present the fabrication process of the metalens and the equipment used throughout the manufacturing procedure. Next, we will combine the fabricated metalens with some optical components to create a miniature near-infrared camera.

We will evaluate the metalens by analyzing its transmission efficiency and determine the quality of the camera through modulation transfer function (MTF) by capturing images of a resolution test chart.

Finally, using this camera, we can perform simple infrared photography and even pupil detection.

3.1 Fabrication of Metalens

3.1.1 Fabrication Process

In this segment, we present a brief overview of the metalens fabrication process and the instruments employed at each stage.

The experiment process is illustrated in Fig. 3-1.

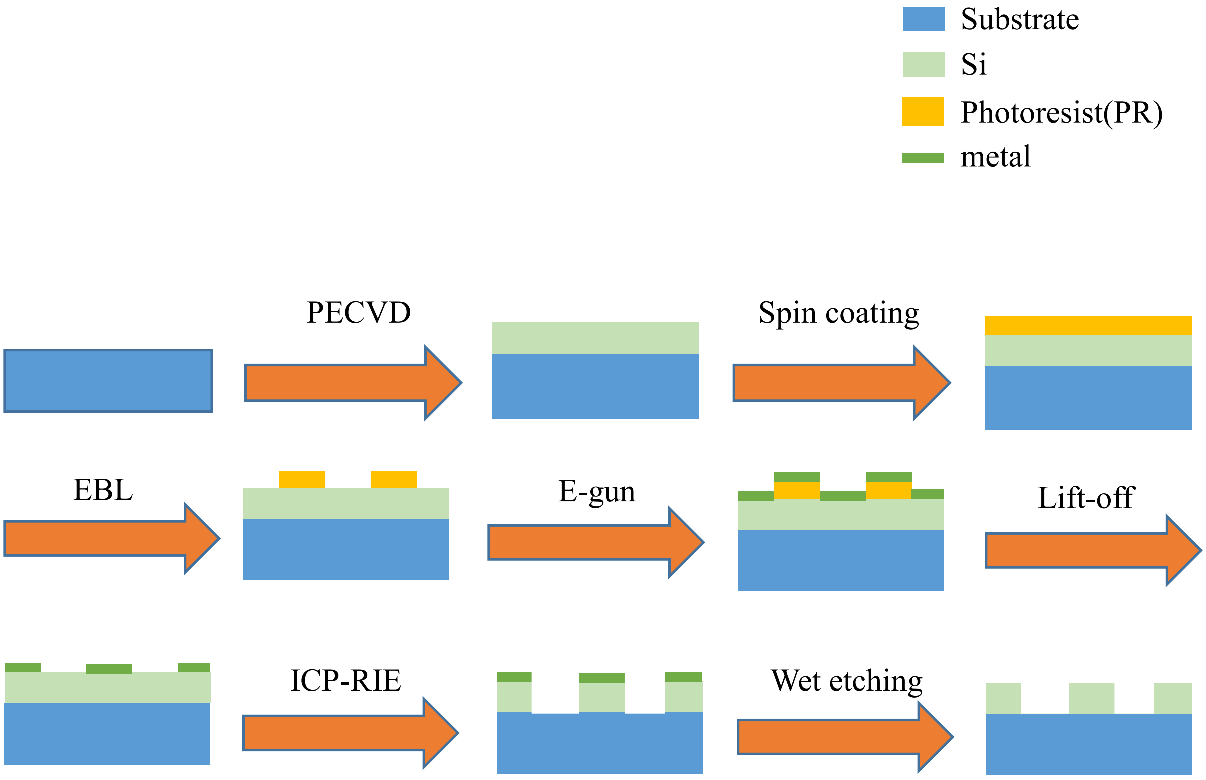

Fig. 3-1 The process flow diagram

First, a 4-inch glass wafer is cut into 1 cm × 1 cm samples to facilitate the experiment. The samples are then cleaned following the method described in Section

2.1. After cleaning, any residual organic substances and moisture on the sample are removed using UV-Ozone. Finally, through PECVD, a layer with a thickness of 570 nm of a-Si is deposited onto the glass substrate, finalizing the epitaxial growth of the silicon.

After the epitaxy, a series of lithography processes are carried out. First, HMDS is applied to the sample, with the spin speed set to 4000 rpm to ensure uniform coating. HMDS enhances the adhesion of the photoresist, improving its stability. Next, a positive photoresist (AR-P6200.09) is applied to the sample, with the spin speed set to 7100 rpm to ensure uniform coverage. Afterward, the sample undergoes a prebake at 130°C for a minute. The sample is then cooled at normal temperature for 1 minute before exposure using EBL to create a metalens with diameter of 1500 μm. After exposure, sample is immersed in AR 600-546 developer for 1 minute to ensure complete development. The sample is subsequently immersed in deionized (DI) water for 1 minute to wash away any remaining developer. Finally, the surface of the sample is dried using a nitrogen air gun, completing the lithography process.

Using Electron Gun Evaporation, 50 nm thick layer of Ni is applied to the sample as a protective layer for subsequent etching. The lift-off process is then employed to shift the pattern from photoresist to Ni layer. Next, ICP-RIE is used for etching, with 30

doi:10.6342/NTU202404691

sccm (standard cubic centimeters per minute) O_2 and 25 sccm SF_6 gases introduced, and the sample is etched for 115 seconds. Finally, the sample is immersed in a solution ($H_2SO_4 : H_2O_2 = 2 : 1$) for 5 minutes to remove the remaining protective Ni layer, completing the fabrication of the metalens.

3.1.2 Equipment of Fabrication

In the process of fabricating the metalens, we used some processing equipment and employed measurement instruments to verify the accuracy of the metalens structure.

In this section, we will give a brief overview to these machines, categorizing them into processing equipment and measurement instruments.

doi:10.6342/NTU202404691

- **Processing Equipment**

1. UV-Ozone

When cleaning glass surfaces, UV-Ozone is commonly used, as it can effectively remove non-contact organic substances at room temperature and atmospheric pressure. The UV-Ozone we use is shown in Fig. 3-2.

Fig. 3-2 UV-Ozone Cleaner (Samco, UV-1).

The UV light source emits photons with energies of 184.9 nm and 253.7 nm. When these photons hit the surface of the object being cleaned, most hydrocarbon compounds strongly absorb the 184.9 nm photons, triggering a photochemical reaction that breaks

doi:10.6342/NTU202404691

them down into ions, free radicals, excited molecules, and neutral molecules. At the same time, oxygen molecules in the air absorb the 253.7 nm photons, generating ozone (O_3) and atomic oxygen (O). Ozone also has strong absorption at 184.9 nm and decomposes into oxygen (O_2) and atomic oxygen (O). The reaction process is presented in Equations 3.1.2.1 to 3.1.2.3 [22].

$$\text{Contaminant Molecules} + h\nu_1 \rightarrow \begin{matrix} \text{Ions} \\ \text{Free Radicals} \\ \text{Excited Molecules} \\ \text{Neutral Molecules} \end{matrix} \qquad (3.1.2.1)$$

$$\mathrm{O_2} + h\nu_2 \rightarrow \mathrm{O}, \mathrm{O_3} \qquad (3.1.2.2)$$

$$\begin{matrix} \text{Ions} \\ \text{Free Radicals} \\ \text{Excited Molecules} \\ \text{Neutral Molecules} \end{matrix} + \mathrm{O}, \mathrm{O_3} \rightarrow \begin{matrix} \text{Volatile Molecules} \\ (\mathrm{CO_2}, \mathrm{H_2O}, \mathrm{N_2}, \text{etc.}) \end{matrix} \qquad (3.1.2.3)$$

Due to the high reactivity of atomic oxygen, it easily combines with carbon and the decomposition products of hydrocarbons on the object’s surface, forming volatile gases including carbon dioxide, oxygen, and water vapor. These gases are easily released from the surface, thoroughly removing carbon and organic contaminants adhering to the object.

doi:10.6342/NTU202404691

2. Plasma-Enhanced Chemical Vapor Deposition (PECVD)

Plasma-Enhanced Chemical Vapor Deposition (PECVD) is an advanced deposition technique used to create thin films by converting material from a gaseous (vapor) phase to a solid phase on a substrate. In PECVD, the process begins with precursor gases being introduced into a vacuum chamber. These gases are then subjected to a plasma field, which is generated by applying an electric field or radiofrequency energy. The plasma creates reactive species, such as ions, radicals, and excited molecules, which interact with the surface of the substrate.

The key feature of PECVD is the "plasma-enhanced" aspect, which allows chemical reactions to occur at lower temperatures than those required in traditional Chemical Vapor Deposition (CVD). In conventional CVD, high temperatures are typically needed to activate the chemical reactions that deposit the material. However, in PECVD, plasma assists in activating these reactions, enabling deposition at lower substrate temperatures. This makes PECVD particularly useful for sensitive materials, like organic substrates or devices that cannot withstand high temperatures, while still producing high-quality thin films for applications in electronics, coatings, and photovoltaic cells.

doi:10.6342/NTU202404691

This process allows precise control over the film's composition, structure, and thickness, making PECVD a popular method for manufacturing semiconductor devices, solar panels, and other high-tech applications.

The PECVD we use is shown in Fig. 3-3.

Fig. 3-3 PECVD

doi:10.6342/NTU202404691

In PECVD, a mixture of gaseous precursors (reactive gases) is introduced into a vacuum chamber where the deposition occurs. These gases are chosen on the basis of the material to be deposited.

A radio frequency (RF) or DC power supply is applied to generate plasma in the chamber. Plasma is a partly ionized gas made up of ions, neutral particles and electrons. The plasma energy breaks down the precursor gases into reactive species like radicals, ions, and atoms.

These reactive species then adhere to substrate surface. Chemical reactions on substrate surface result in formation of a thin solid film. Unlike thermal CVD, PECVD Utilizes plasma to supply the energy for the reaction, allowing deposition at lower temperatures (typically 100–400℃).

The substrate is typically heated, albeit at significantly lower temperatures than traditional CVD processes. The low-temperature deposition is one of the major advantages of PECVD, enabling the coating of temperature-sensitive materials like polymers.

Process parameters, involving RF power, temperature, chamber pressure, and gas flow rates are adjusted to regulate the film's composition, thickness, and properties.

Therefore, PECVD has the advantages of low temperature, conformal coatings, wide range of materials, and enhanced film properties. It offers the flexibility to deposit high-quality thin films on a broad spectrum of materials and extensively utilized in industries requiring precise, controlled film growth at lower temperatures.

3. Spin Coater

A spin coater is a tool designed to spread uniform thin films onto substrates using the spin coating process. This technique is generally used in industries such as manufacturing, photolithography, and material science to deposit layers of photoresists, polymers, or other coatings. The spin coater we use is shown in Fig. 3-4.

doi:10.6342/NTU202404691

Fig. 3-4 Spin Coater (Mikasa, Opticoat MS-A100).

The substrate (e.g., a silicon wafer, glass slide) is put on a chuck. The chuck holds the substrate in place, often using vacuum suction to ensure stability during spinning.

A small quantity of coating solution (liquid material to be deposited) is applied to the center of the substrate. The amount of solution used relies on the material's viscosity and desired film thickness.

Spin coater starts to rotate at controlled speed, which spreads the solution across the surface of the substrate due to centrifugal force. The spinning causes the solution to spread uniformly from the center to the edges.

As the sample rotates, the centrifugal force drives the liquid to disperse outward, creating thin film across the substrate. The thickness of the film decreases with increasing spin speed.

During spinning, solvent from the solution evaporates, which aids in the formation of a solid thin film. Higher spinning speeds tend to result in thinner films because more liquid is expelled from the substrate.

Several parameters influence the final thickness of the film: spin speed, spin duration, viscosity of solution, dispensed volume.

After spinning, the substrate may undergo further processing, such as baking or curing, to ensure that the coating is fully dried or chemically modified for better adhesion or film properties.

Therefore, spin coater has the advantages of uniformity, time consumption is very low, thickness control is precise, cost-Effective. It is a simple yet highly effective method for creating thin films with accurate control over thickness and consistency.

doi:10.6342/NTU202404691

4. Electron-beam Lithography (EBL)

The principles of electron-beam lithography and an introduction to the instrument are provided in detail in Section 2.2.2 of this thesis, so they will not be further elaborated here.

5. Electron Gun Evaporation

Electron Gun Evaporation (or Electron Beam Evaporation) is a physical vapor deposition (PVD) technique employed to deposit thin films onto substrates by heating a source material using a focused electron beam. The electron beam provides the energy needed to evaporate the material. This material then condenses onto the substrate, forming a thin film. It usually includes an electron gun, crucible, vacuum chamber, and substrate holder. The electron gun evaporation we use is shown in Fig. 3-5.

Fig. 3-5 Electron Gun Evaporation

The process takes place within a vacuum chamber, which reduces contamination and prevents collisions between evaporated particles and air molecules, ensuring a clean deposition. High vacuum (10^{-5} to 10^{-7} Torr) is typically maintained.

An electron gun, usually positioned outside the evaporation crucible, generates a concentrated beam of high-energy electrons. Electrons are accelerated by an electric field and directed toward the target material using magnetic fields.

The focused electron beam is aimed at the surface of the objective material (also known as the evaporation source, especially for metals.). Beam's energy warms the material resulting it in reach evaporation point.

As the target material heats up, it begins to vaporize. The vaporized atoms or molecules escape from the material's surface and move towards the cooler substrate positioned above the evaporation source.

The vaporized particles settle on the substrate and condense, forming a thin film. Film thickness can be regulated by modifying the deposition time, electron beam power, and distance between source and substrate.

Electron beam can efficiently heat materials with high melting points (e.g., metals like tungsten, titanium, and gold), which are challenging to vaporize with conventional thermal evaporation methods. This makes it suitable for depositing metals, oxides, and other high-temperature materials.

Therefore, electron gun evaporation has the advantages of high deposition rates, high-purity films, ability to evaporate high melting point material, good control over film thickness. It is a versatile, efficient, and widely used thin-film deposition method, particularly suitable for high-purity coatings and high melting-point materials.

doi:10.6342/NTU202404691

6. Inductively Coupled Plasma-Reactive Ion Etching (ICP-RIE)

Inductively Coupled Plasma-Reactive Ion Etching (ICP-RIE) is a sophisticated etching technique used in semiconductor manufacturing and microfabrication. It integrates the benefits of both reactive ion etching (RIE) and inductively coupled plasma (ICP) to achieve high etch rates and excellent etch uniformity. The instrument we use is illustrated in Fig. 3-6.

Fig. 3-6 Inductively Coupled Plasma-Reactive Ion Etching (ICP-RIE)

doi:10.6342/NTU202404691

Procedure takes place in a vacuum chamber, where a low-pressure environment (typically between 1 and 20 mTorr) is maintained to reduce contamination and improve etching characteristics.

Reactive gases (etching gases) are introduced into the vacuum chamber. These gases typically include fluorinated gases (such as SF_6, CF_4, or CCl_4) and sometimes oxygen or other gases, depending on the materials being etched.

An inductive coil wrapped around the vacuum chamber generates a high-frequency (usually RF) electromagnetic field. When RF power is applied, it generates a magnetic field, which in turn creates an electric field in the gas. This process ionizes the gas, producing a dense plasma of neutral species, electrons, and ions.

Inductively coupled plasma (ICP) produces a high density of ions compared to traditional capacitively coupled plasma systems. The high ion density results in better control over the etching process. The etching mechanism can be divided into two regions: ion bombardment (physically) and chemical reactions (chemically).

- Ion Bombardment: Ions produced in the plasma are directed towards the substrate surface. When these ions collide with the surface, they physically bombard and sputter away the material, contributing to the etching process.
- Chemical Reactions: Reactive species in plasma chemically react to the material on the substrate, forming volatile byproducts that are then pumped out of the chamber. This combination of physical and chemical processes enhances etching efficiency.

By adjusting the power levels, gas flow rates, and pressure in the chamber, the etch rate and profile can be finely controlled. ICP-RIE allows for anisotropic etching, meaning the etching is directional and can create well-defined vertical sidewalls.

The substrate is typically mounted on a powered electrode (the substrate holder), which can also be heated or cooled to control the temperature during the process of etching.

Therefore, inductively coupled plasma-reactive ion itching (ICP-RIE) has the advantages of high etch rates, excellent anisotropy, versatility, uniformity. It is a powerful and essential technique in modern microfabrication, providing high precision and flexibility in the etching process.

doi:10.6342/NTU202404691

■ Measurement Instruments

1. Scanning Electron Microscopy (SEM)

Scanning Electron Microscopy (SEM) is an advanced imaging technique utilized for analyzing the surface morphology and composition of samples at high magnifications. In contrast to conventional light microscopy, SEM uses electrons instead of light to form images, which allows for much higher resolution. The scanning electron microscopy we use is shown in Fig. 3-7.

Fig. 3-7 Scanning Electron Microscopy (SEM)

The SEM utilizes a concentrated beam of high-energy electrons produced by an electron gun, usually composed of a tungsten filament or a field emission emitter. When the filament is heated, it emits electrons, which are then accelerated and focused into a narrow beam.

The electron beam is focused with the help of electromagnetic lenses, which are utilized to regulate the beam's convergence and spot size. This focused beam is directed towards surface of sample.

When electron beam strikes sample, various interactions take place:

- Secondary Electrons: The surface of the sample emits low-energy electrons upon interaction with the electron beam. These secondary electrons serve as the main source of contrast in SEM images.
- Backscattered Electrons: Some of the incident electrons are reflected back from the sample surface. These backscattered electrons can provide information about the sample's atomic number and topography.
- Characteristic X-rays: High-energy electrons can also induce inner-shell ionization of atoms in the sample, resulting in the emission of characteristic X-rays, which can be analyzed for compositional information.

The secondary and backscattered electrons are captured by detectors:

doi:10.6342/NTU202404691

- Secondary Electron Detector: This detector captures low-energy secondary electrons, producing high-resolution images of the sample's surface.
- Backscattered Electron Detector: This detector collects backscattered electrons to provide additional contrast based on the atomic composition of the sample.

The detected signals are converted into electrical signals, which are then processed to form an image. The intensity of the identified signals correlates with topography and composition of sample, resulting in detailed images.

The electron beam is scanned across sample surface in a systematic raster pattern (line by line), allowing for the creation of a two-dimensional image of the sample.

SEM operates in a vacuum chamber to prevent electron scattering by air molecules, ensuring high-resolution imaging and reducing sample contamination.

Therefore, Scanning Electron Microscopy (SEM) has the advantages of high resolution, depth of field, material characterization**.** It is a versatile and essential tool in many scientific fields. This process provides high-clarity images and valuable insights into morphology and composition of different materials.

doi:10.6342/NTU202404691

3.2 Measurement setup

With the completion of the metalens fabrication, we will use several optical measurement methods to evaluate the quality of the metalens.

First, we will use a 940nm infrared laser as light source to measure focusing efficiency of metalens. We direct the laser into the distant aperture, setting the diameter of the aperture to 1 mm to ensure that the distance from the laser to the aperture is collimated. A schematic of collimated setup is presented in Fig. 3-8. Next, we pass the laser through the aperture, set the aperture diameter to 2 mm, and direct the beam into the metalens, ensure that the laser beam incident on the metalens is appropriate. This allows for the precise measurement the focusing efficiency. By measuring the beam's power at the focal point and comparing it to the power before the beam passes through the metalens, we can calculate the focusing efficiency. A schematic of measuring the focusing efficiency is shown in Fig. 3-9. Next, we replaced the power meter with a CMOS sensor to measure light intensity distribution. A schematic of measuring light intensity distribution is demonstrated in Fig. 3-10.

doi:10.6342/NTU202404691

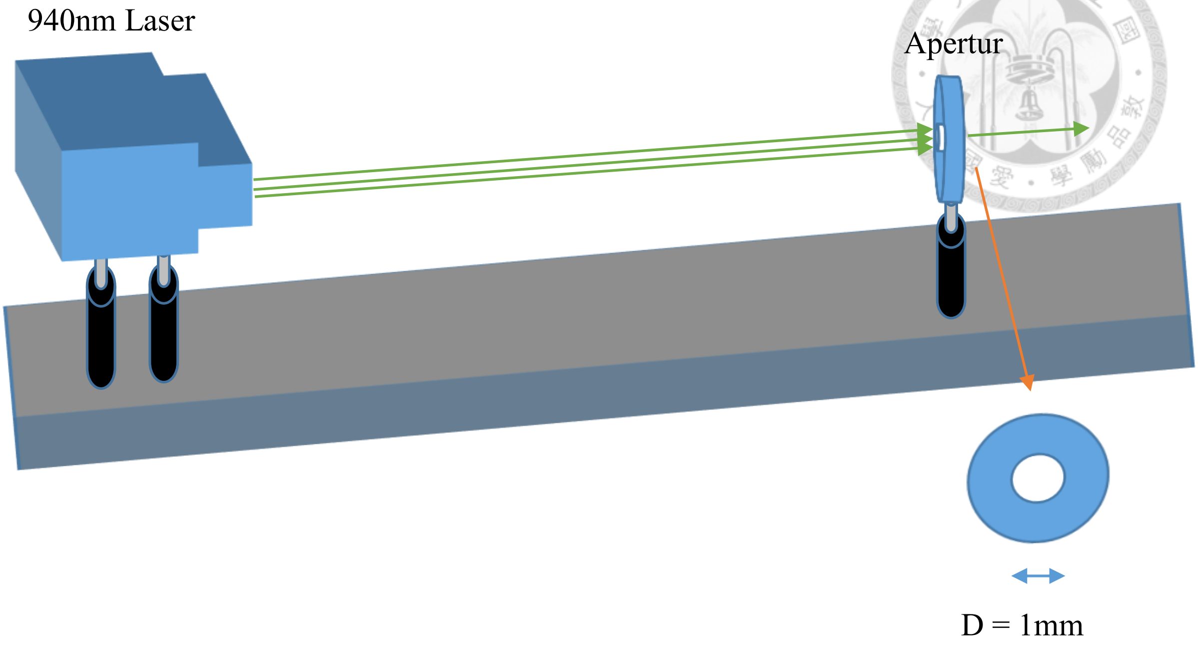

Fig. 3-8 The schematic for collimated.

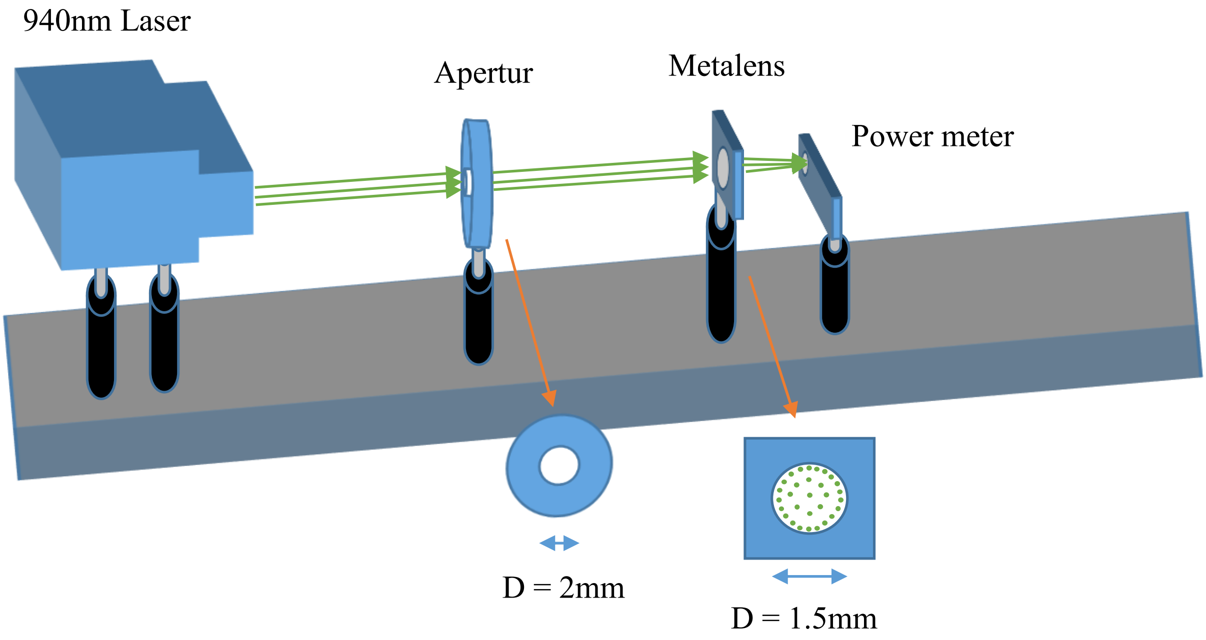

Fig. 3-9 The schematic of measuring the focusing efficiency.

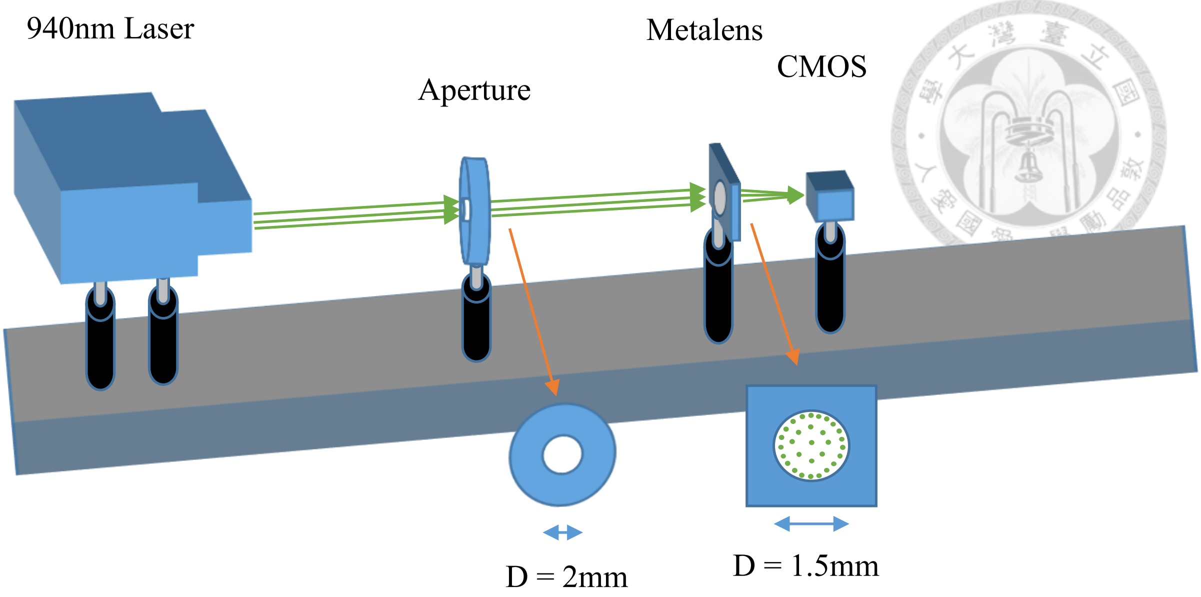

Fig. 3-10 The schematic of the measuring the light intensity distribution of the metalens.

Next, we will switch the light source to a 940nm LED, shining the light directly onto a resolution target. The reflected light will be focused through the metalens onto a CMOS sensor, capturing images of a resolution target. By performing image analysis, we will generate an MTF (Modulation Transfer Function) chart to assess the quality of the infrared miniature camera created by combining the metalens and the CMOS sensor. A diagram of experimental setup for capturing images is illustrated in Fig. 3-11, while actual setup is illustrated in Fig. 3-12.

doi:10.6342/NTU202404691

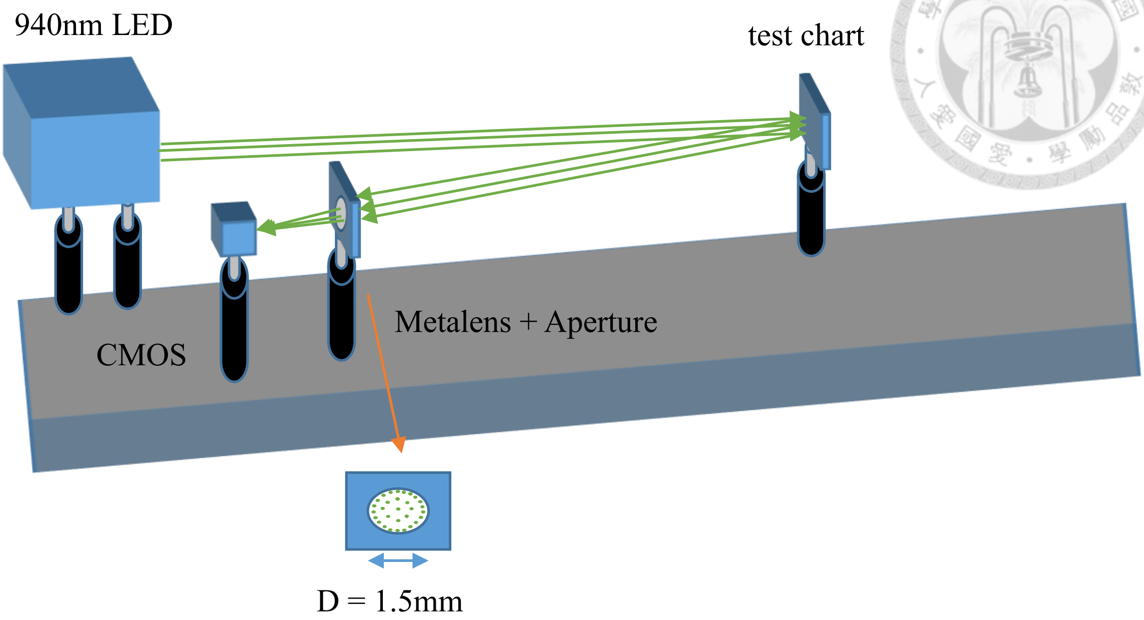

Fig. 3-11 The schematic for capturing images of resolution target.

doi:10.6342/NTU202404691

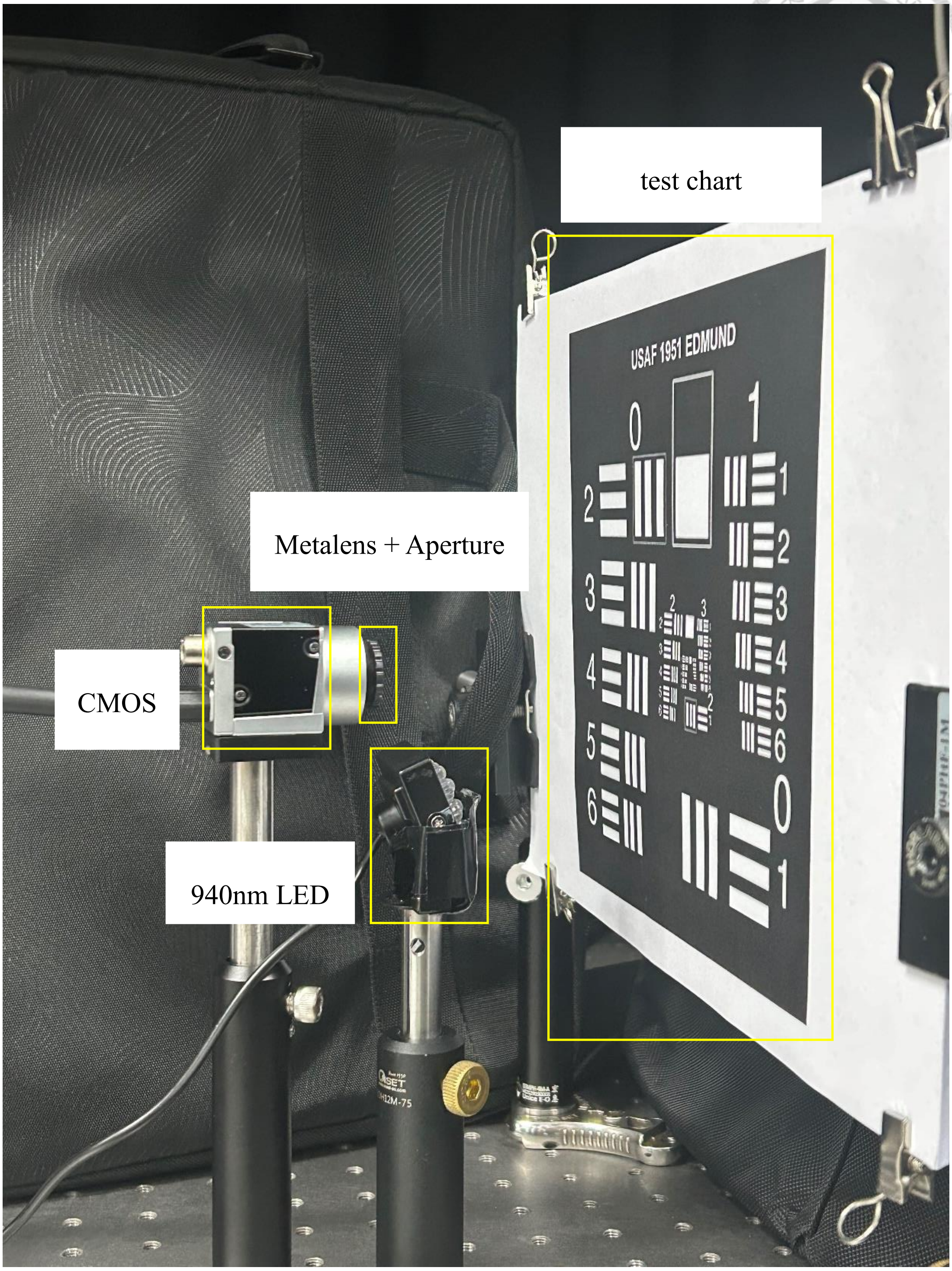

Fig. 3-12 The experiment setup for capturing images of resolution target.

doi:10.6342/NTU202404691

Finally, we will replace the resolution test target with a human eye. The reflected light will pass through the metalens and focus on the CMOS sensor to produce a photograph of human eye. A schematic for capturing images of human eye is illustrated in Fig. 3-13, while actual setup is illustrated in Fig. 3-14.

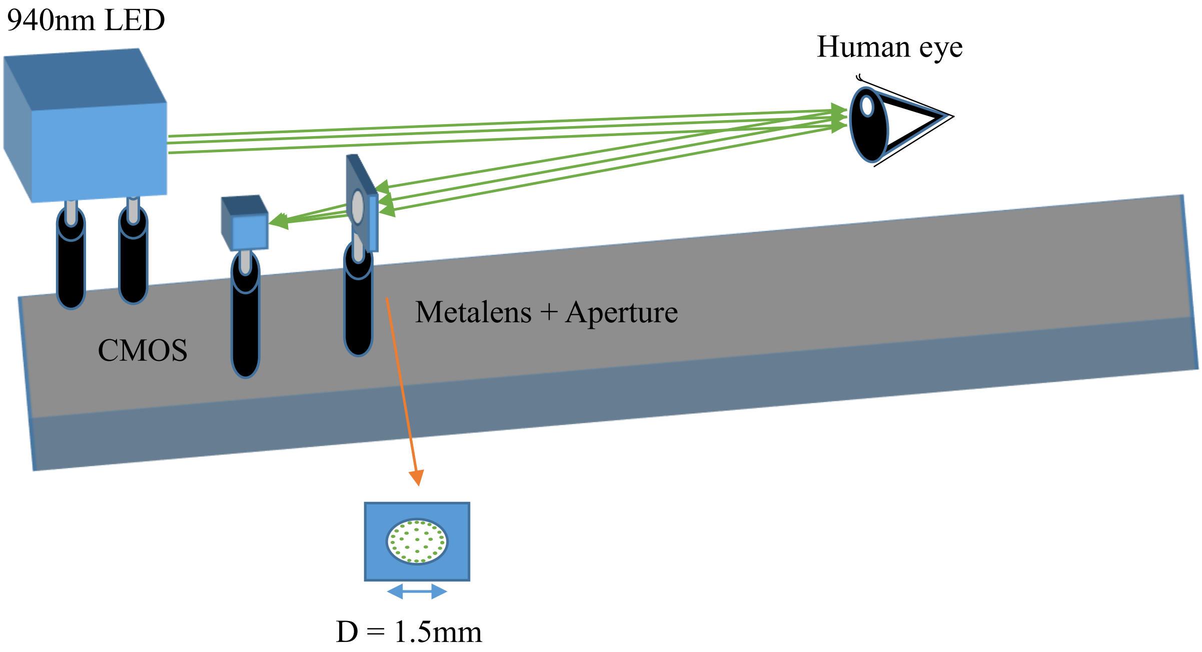

Fig. 3-13 The schematic for capturing images of the human eye.

doi:10.6342/NTU202404691

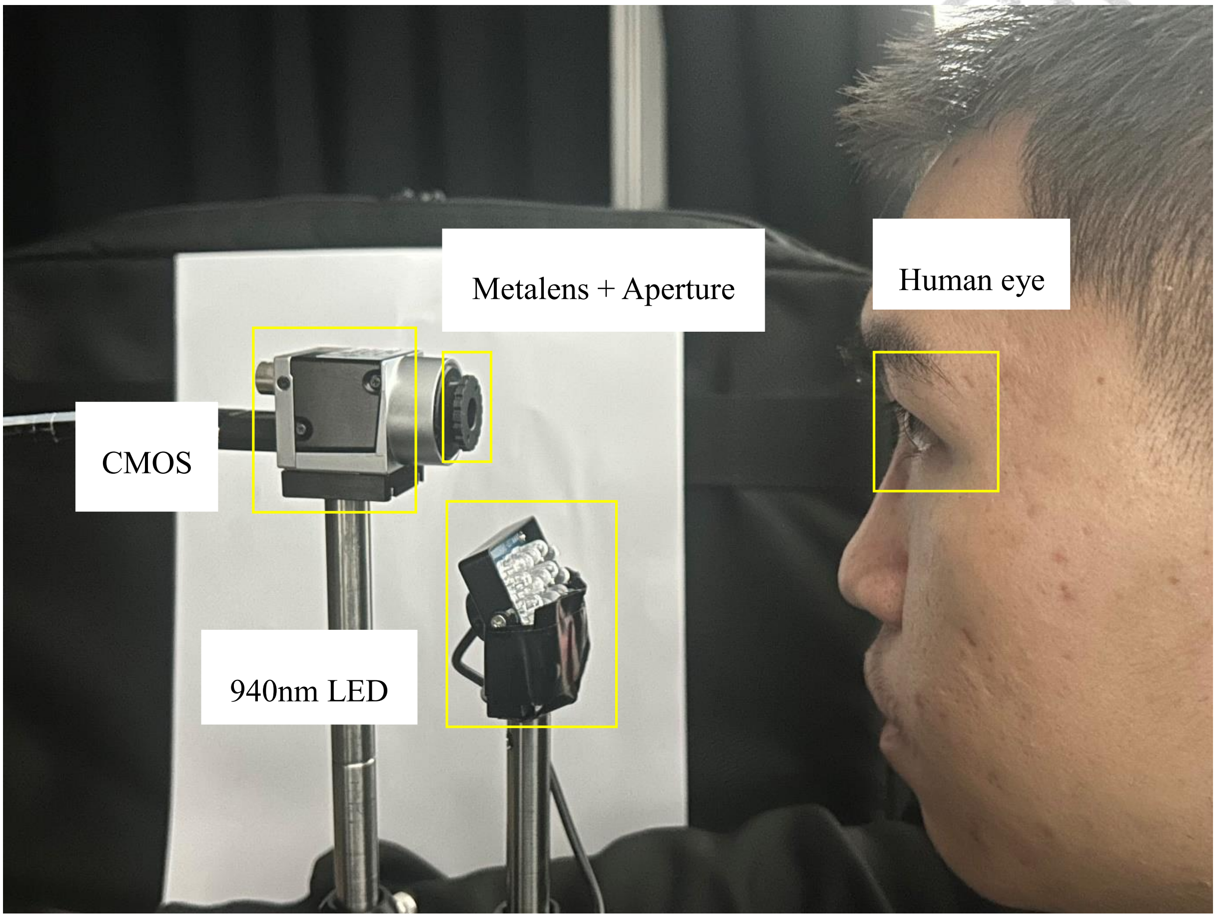

Fig. 3-14 The experiment setup for capturing images of the human eye.

This design could potentially be used in wearable devices such as AR/VR glasses or even in miniature medical equipment in the future.

doi:10.6342/NTU202404691

Chapter 4 Experiment Data and Results

In this section, we will analyze the experimental results obtained from each step of the semiconductor fabrication process. Then, using the optical measurement methods mentioned in Chapter 3, we will evaluate the quality of the metalens itself and assess the imaging capabilities of an infrared micro-camera formed by integrating the metalens with CMOS. Finally, through this optical system, we can achieve the purpose of pupil detection.

4.1 Fabrication of Metalens

4.1.1 Substrate Cleaning

In principle, as described in Section 2-1, the cleaning method can ensure a high success rate of depositing a-Si on a glass substrate. However, in some cases during the lift-off process, the deposited a-Si may detach along with the lift-off solution, similar to the detachment of metal (Ni) deposited on the photoresist.

This issue occurs due to incomplete removal of organic substances during glass substrate cleaning, leaving minor organic residues on the substrate. Consequently, instead of depositing directly on the glass, the a-Si is deposited on these organic residues.

doi:10.6342/NTU202404691

As a result, during the lift-off process, the a-Si is removed along with the organic material, similar to metal on photoresist. Flowchart of cleaning process is displayed in Fig. 4-1, where (a) represents the ideal cleaning process and (b) shows the defective cleaning process.

To reduce the occurrence of defects, UV-Ozone treatment can be applied after cleaning the glass substrate. This approach significantly reduces the probability of organic residues remaining on the glass, thereby improving the success rate of a-Si deposition and the overall success rate of metalens fabrication.

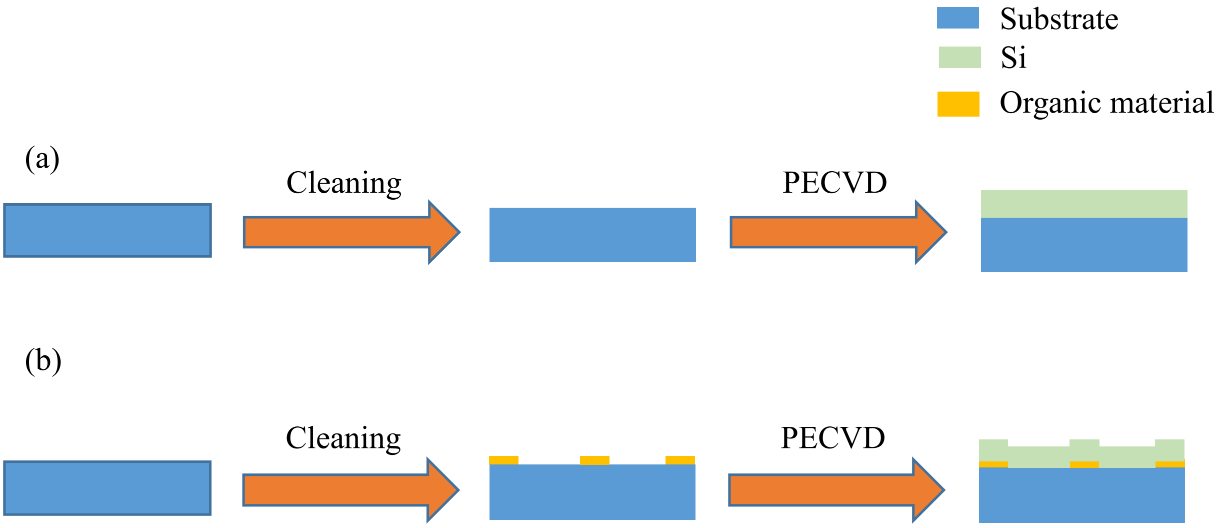

Fig. 4-1 The cleaning process of ideal (a) and defective (b).

doi:10.6342/NTU202404691

4.1.2 Photoresist pattern by Lithography

After a series of lithography processes, once the pattern emerges through development, we can observe it using an optical microscope (OM) and a scanning electron microscope (SEM). By comparing observed pattern with original design (GDS file), we can assess the quality of the lithography process.

Fig. 4-2 and 4-3 show the original design of the metalens (GDS file): Fig. 4-2 displays the entire metalens, while Fig. 4-3 provides a close-up view, highlighting the fine nanopillar structures within.

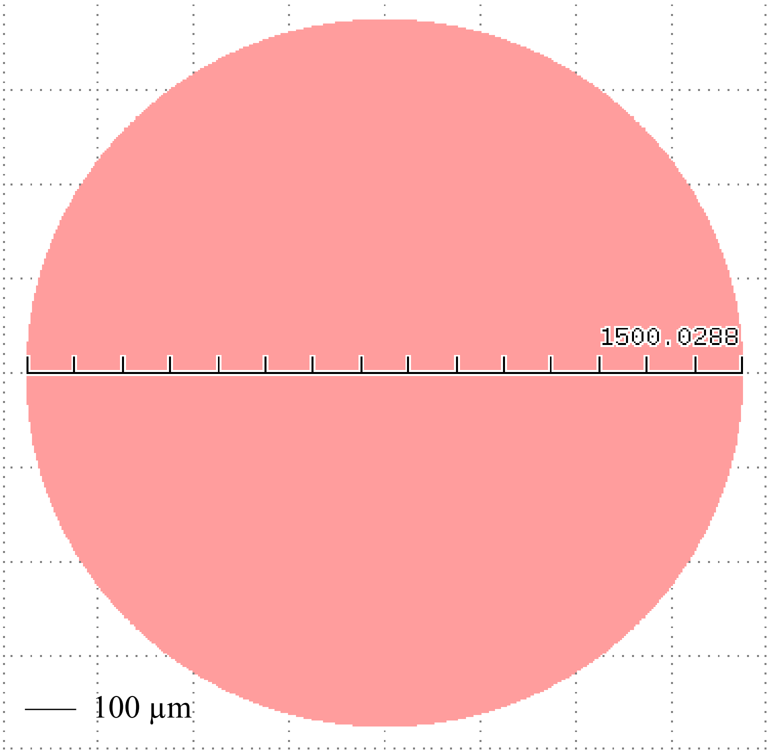

Fig. 4-2 GDS file of a metalens with a diameter of 1500 µm

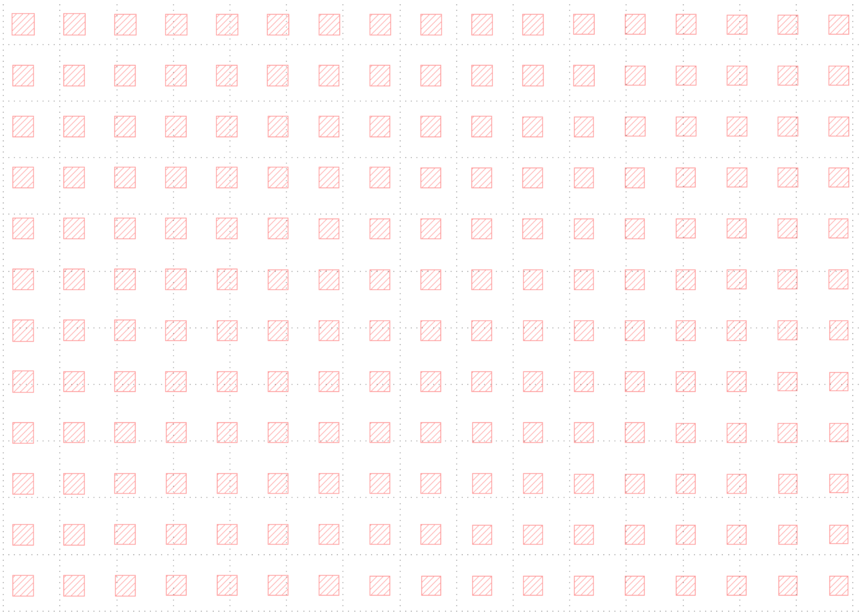

Fig. 4-3 GDS file of numerous nanopillars inside the metalens

During fabrication, various factors may cause defects in the metalens. The most common defects arise from human factors or instability in the equipment. Human contact can easily lead to partial damage, as shown in Fig. 4-4. Equipment instability often causes misalignment, as illustrated in Fig. 4-5 and 4-6. Additionally, insufficient exposure may result in internal pattern deformation or unwanted connectivity, as seen in Fig. 4-7 and 4-8. In rare cases, unclear development may occur, as shown in Fig. 4-9.

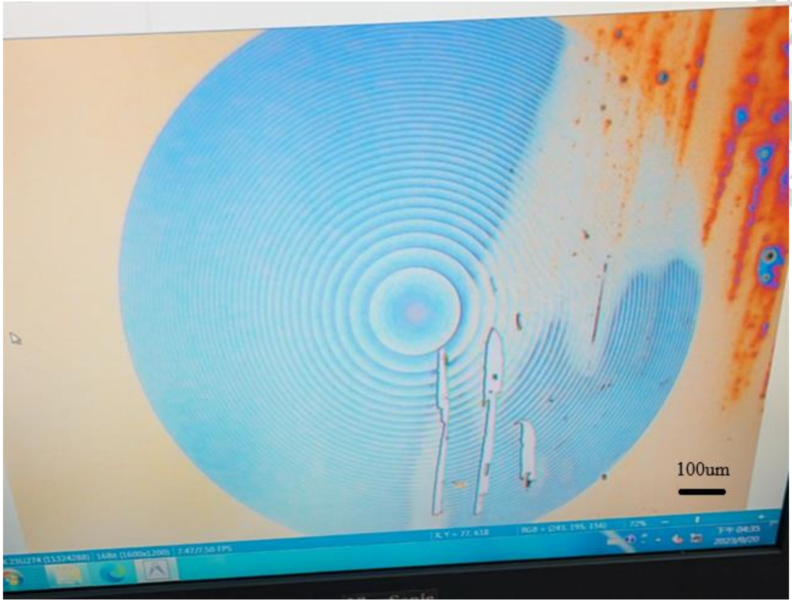

Fig. 4-4 Partial structures are damaged (OM).

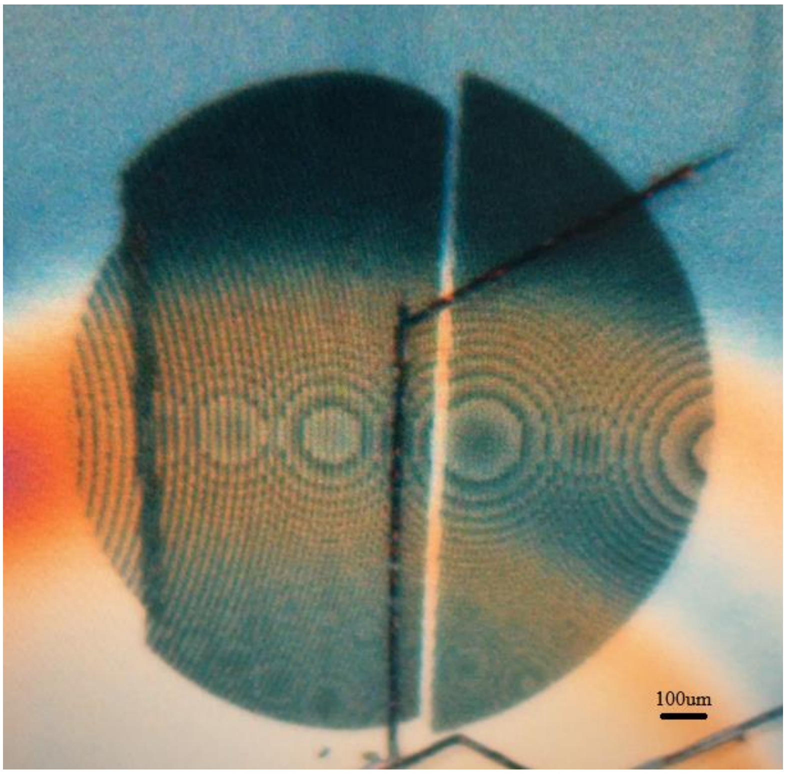

Fig. 4-5 Partial misalignment has occurred (OM).

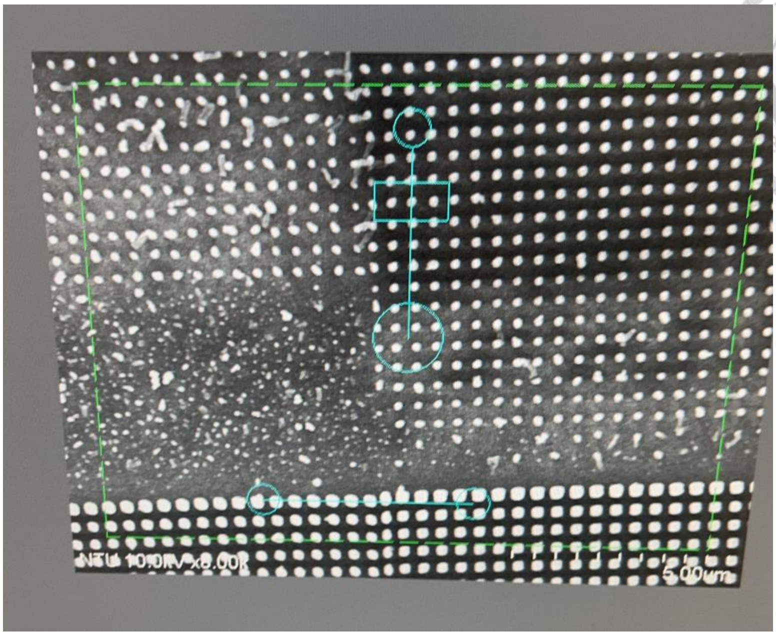

Fig. 4-6 Partial misalignment of the nanopillars has occurred (SEM).

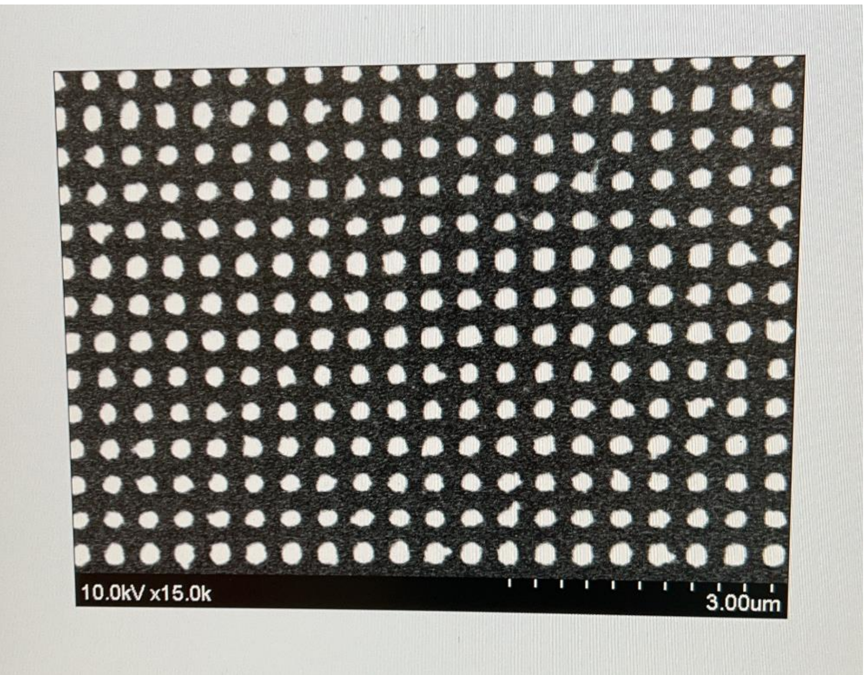

Fig. 4-7 Pattern deformation of the nanopillars has occurred (SEM).

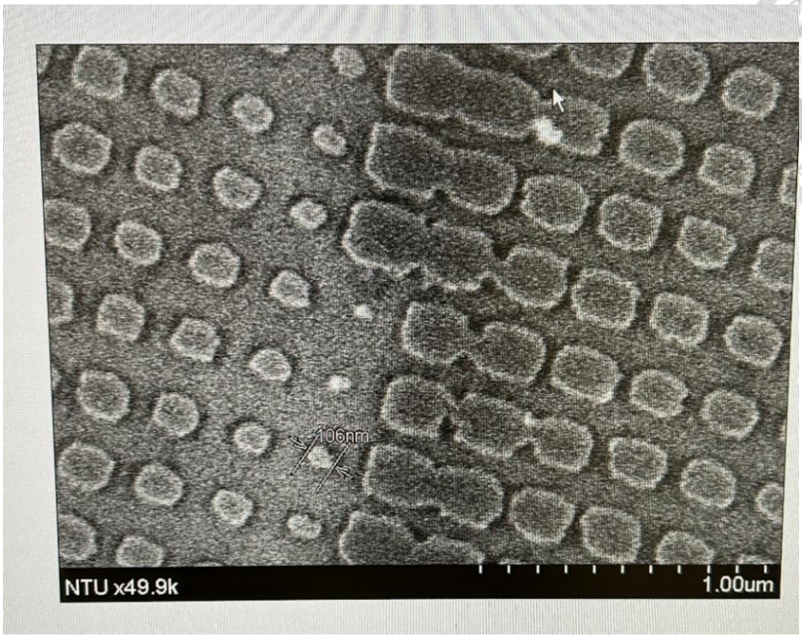

Fig. 4-8 Pattern with unwanted connectivity has occurred (SEM).

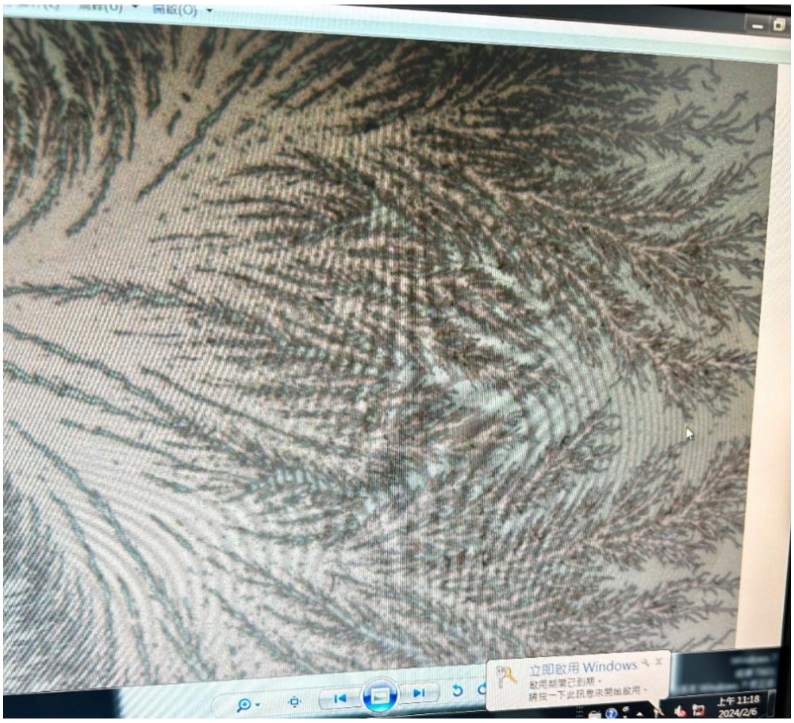

Fig. 4-9 Unclear development has occurred (OM).

When the fabricated metalens does not exhibit these issues, it closely matches the design. Fig. 4-10, 4-11, and 4-12 show experimentally fabricated metalenses. Fig. 4-10 presents the full metalens observed under OM, Fig. 4-11 shows the full metalens viewed under SEM, and Fig. 4-12 provides an SEM close-up of the internal structures of metalens.

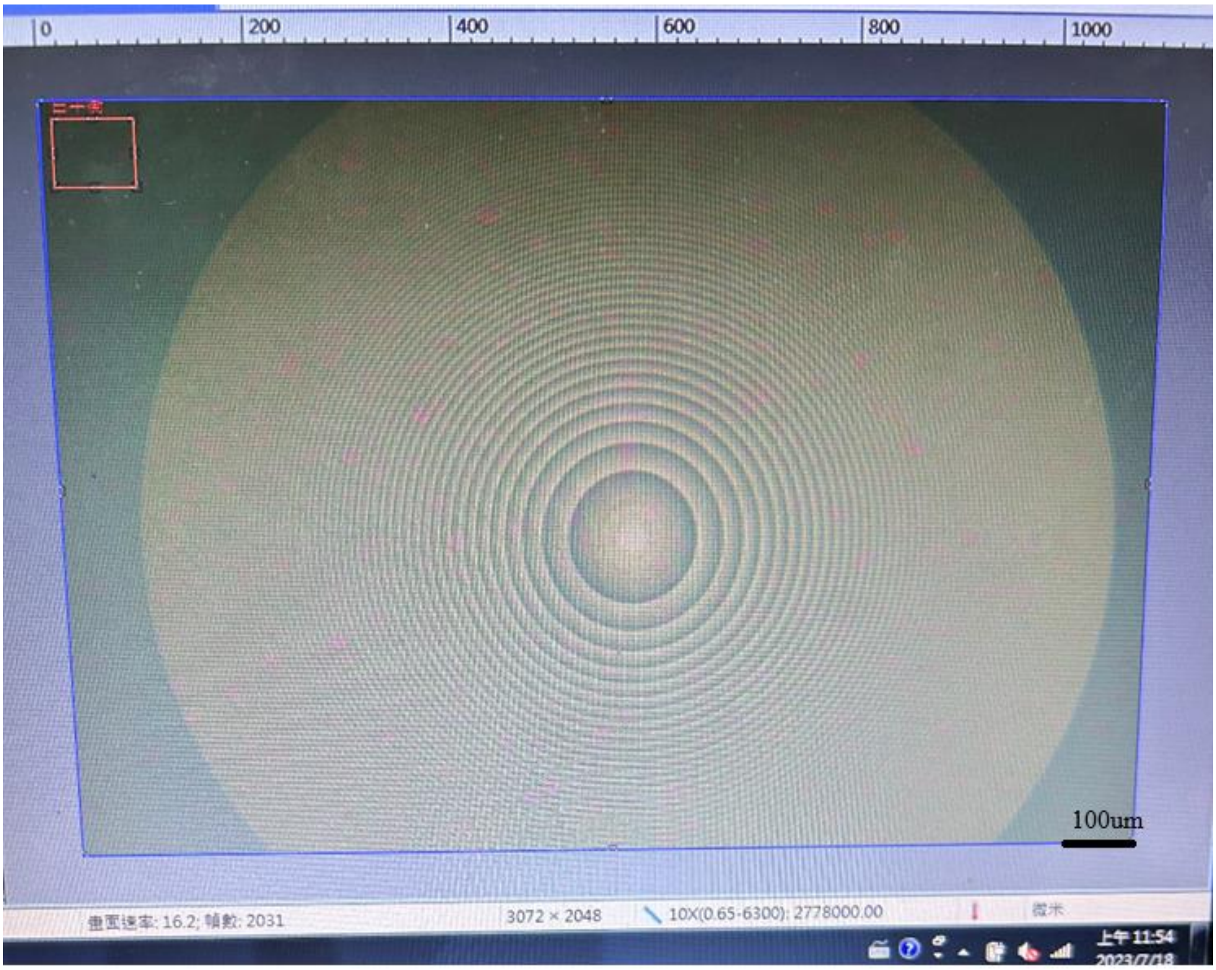

Fig. 4-10 full metalens (OM).

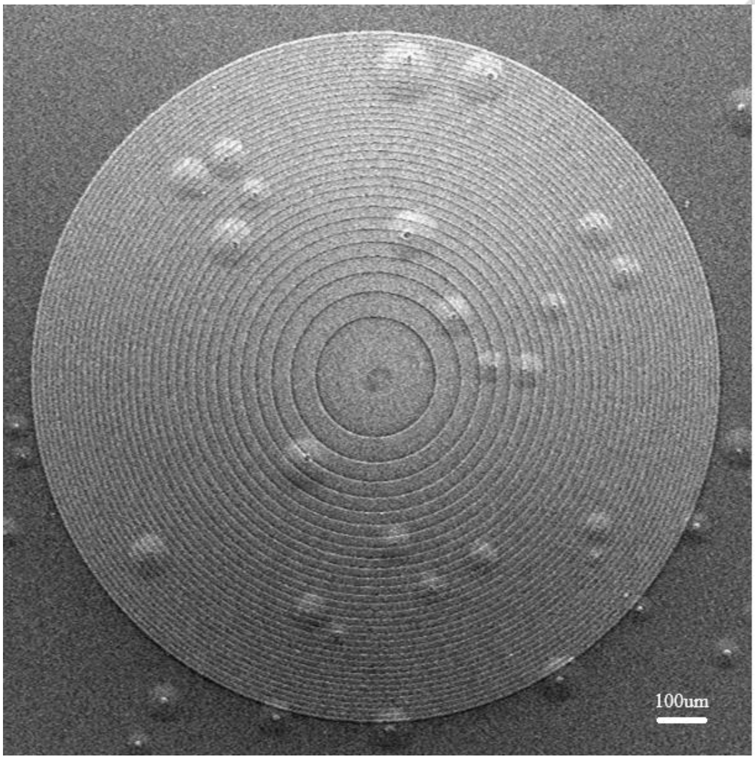

Fig. 4-11 full metalens (SEM).

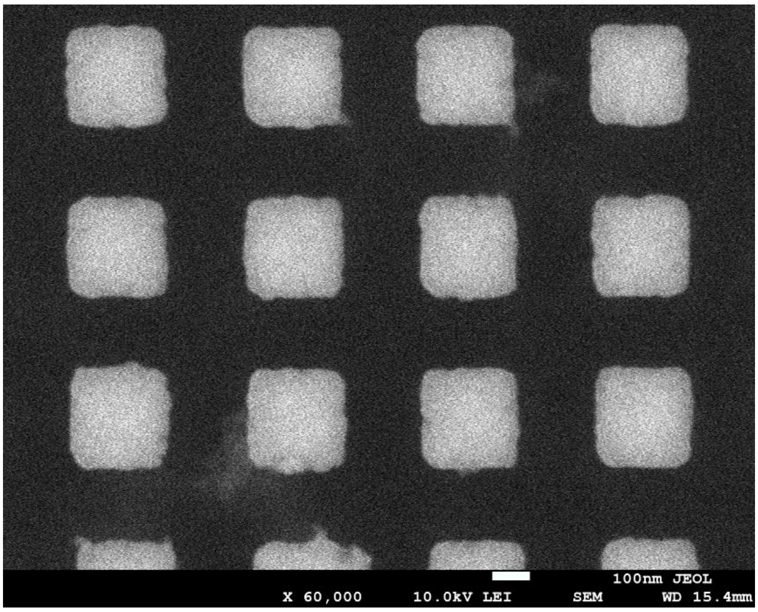

Fig. 4-12 The internal structures of metalens (SEM).

4.1.3 Etching Process with ICP-RIE and Wet Etching

After completing the photolithography process, we use the Electron Gun Evaporation machine mentioned in Section 3.1.2 to deposit a layer of metal (Ni) onto the photoresist, forming a protective layer required for subsequent etching. The pattern on the photoresist is then transferred to this protective Ni layer using the lift-off process described in Section 2.3, followed by dry etching (ICP-RIE).

During the etching process, the Ni protective layer blocks the bombardment of energetic ions, preventing the underlying a-Si from being etched. Conversely, the a-Si areas not protected by the Ni layer are bombarded and etched, with the etching depth determined by the duration of the etching process—the longer the etching time, the deeper the etch.

In the etching of solid silicon (Si), fluoride ions (F) in gaseous form are used due to their strong oxidative properties. Since free F ions are rarely found in nature, they typically exist as F_2 molecules (gas) or in fluorine-containing compounds such as SF_6, CF_4 or CHF_3. However, due to the toxicity of F_2 and the hazardous, costly process required to separate F_2 into reactive F ions, fluorine-containing compounds are commonly used for etching Si in semiconductor processes. When F ions come into contact with Si atoms, a chemical reaction occurs, forming gaseous SiF_4, as shown in the following reaction:

doi:10.6342/NTU202404691

$$Si_{(s)} + 4F_{(g)} \rightarrow SiF_{4(g)} \tag{4.1.3.1}$$

Since the produced SiF_4 is gaseous, it diffuses into the chamber. To sustain the reaction rate equilibrium, more Si atoms will continue to react until the chemical reaction rate reaches equilibrium (i.e., when the supply of fluorine ions is stopped). As a result, the surface Si atoms are gradually reduced, resulting in the gradual etching of the sample.

Following the initial etching, the sample surface starts to display etched grooves. Since the etching process is chemical and non-selective, it is isotropic [23]. To protect the internal sidewalls of these grooves from further etching by reactions between Si and F ions, we introduce O_2. This reacts with Si to form SiO_x ($x = 0, 1, 2, ……$) which shields the inner Si from contact with F ions, creating a selective etching target and achieving anisotropy [24]. By controlling the concentration of O_2, the etching can be directed downward as much as possible [25].

After experimentation, we opted to use SF_6 and O_2 as etching gases in the chamber, with flow rates of 30 sccm and 28 sccm, respectively. The HF power (RIE) is set to 180 W, ICP power (ICP) to 500 W, and pressure set to 25 mTorr, balancing the RIE and ICP etching ratios to achieve the desired nanopillar height. The etching rate is 200 nm per 30 seconds, with a total etching time of 115 seconds reaching a height of approximately 570 nm.

doi:10.6342/NTU202404691

Once the dry etching is complete, sample is dipped in a mixed mixture of H_2SO_4 and H_2O_2 in a 2:1 ratio (H_2SO_4: H_2O_2 = 2:1) for 5 minutes to remove the Ni protective metal layer, thus completing the metalens fabrication.

When the power settings for RIE and ICP are set too high, over-etching can easily occur, leading to the collapse of the nanopillar, as shown in Fig. 4-13. Conversely, if the power is set too low, under-etching may happen, resulting in an etch height that does not meet expectations, as shown in Fig. 4-14. If the power is appropriately set, an etch height consistent with expectations will be achieved, as shown in Fig. 4-15.

The photo was taken at a 45-degree tilt, so the actual height is the measured height $*\sqrt{2}$, Fig. 4-16 shows the schematic diagram of the nanopillar height. The picture taken by SEM is shown in Fig. 4-17.

The actual height of nanopillar is 567 nm (400.781nm $*\sqrt{2}$ = 566.790nm).

doi:10.6342/NTU202404691

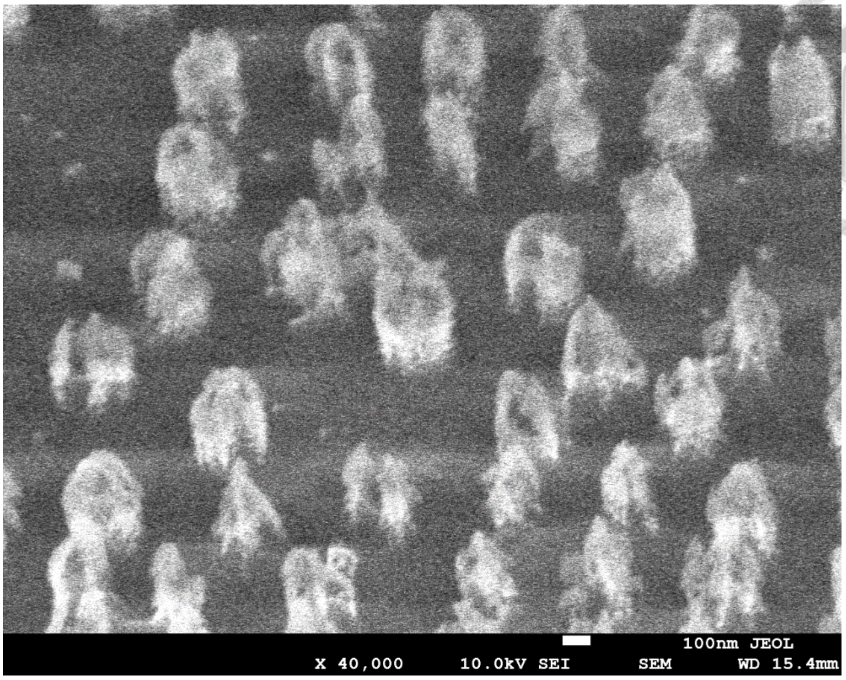

Fig. 4-13 The collapse of the nanopillar

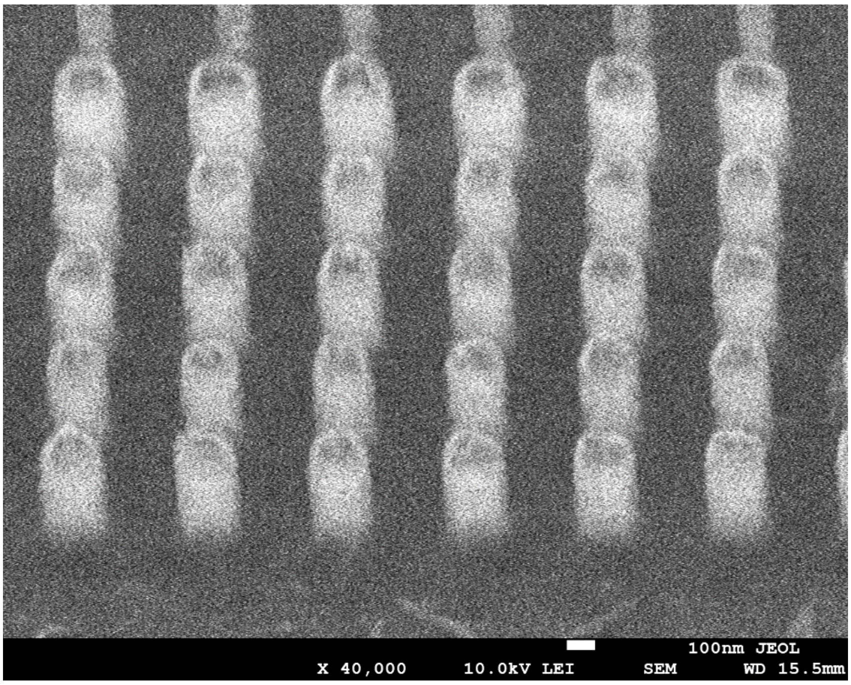

Fig. 4-14 The nanopillar height is too low

doi:10.6342/NTU202404691

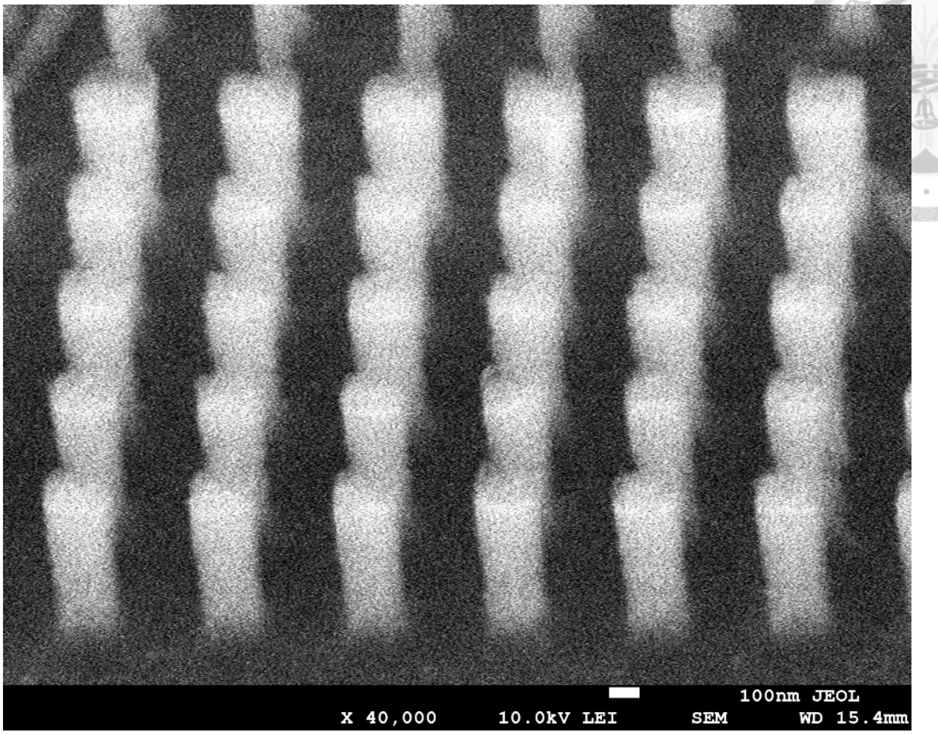

Fig. 4-15 The nanopillar height is appropriate.

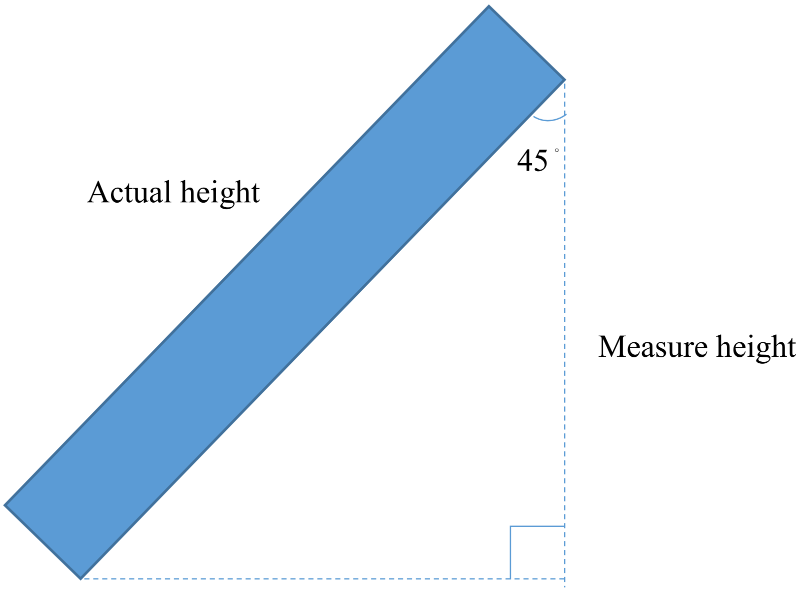

Fig. 4-16 The schematic diagram of nanopillar height.

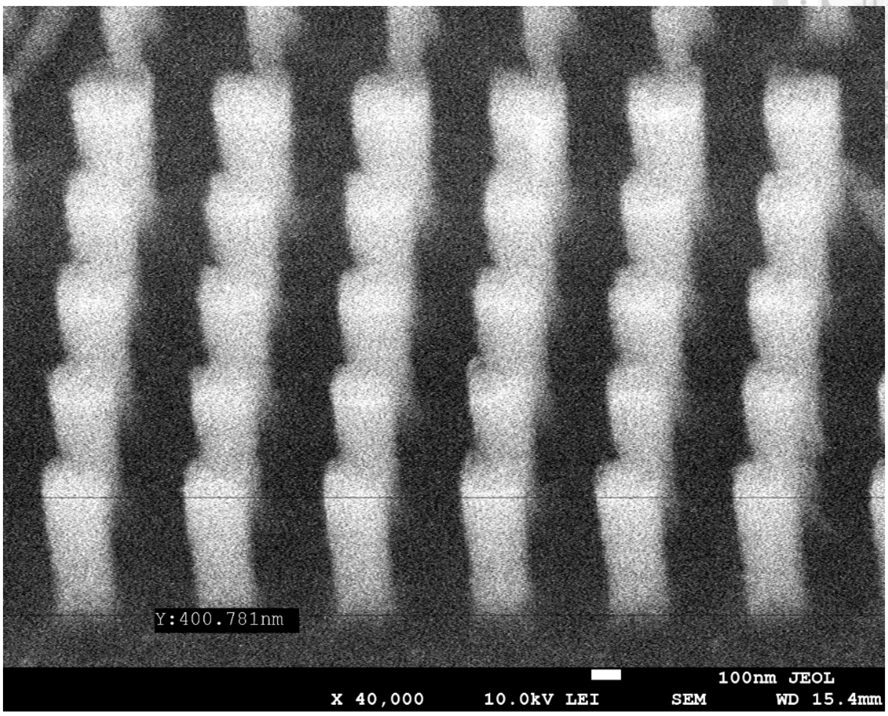

Fig. 4-17 the picture of nanopillar height taken by SEM.

4.2 Measurement and analysis of Metalens

Through a series of manufacturing processes, we produced a metalens with diameter of 1500 μm. To ensure quality of fabricated metalens and micro-camera, which combines the metalens with the integrated CMOS sensor, we apply the method outlined in Section 3.2. First, we use a 940 nm laser as the light source, which is in near-infrared spectrum and outside visible spectrum of human eye. Therefore, we first use a CMOS sensor to observe the focusing behavior of the infrared light through metalens and to measure actual focal length.

doi:10.6342/NTU202404691

The actual focal length measured to be approximately 4500 μm.

Then, a power meter is used to measure the power of 940 nm laser after it has been focused by the metalens. By comparing this to the emitted power of the 940 nm laser, we can determine the focusing efficiency. The focusing efficiency can be calculated using the following formula:

$$\text{Efficiency (\%)} = {}^{\text{Transmitted power } (mW)}\!\big/_{\text{Incident power}(mW)} \quad (4.2.1)$$

After measurement with the power meter, the focusing efficiency is approximately 61.4%. The data for focusing efficiency is shown in Table 4-1.

Initial Efficiency(mW)	Final Efficiency(mW)	Focus Efficiency(%)	Average Efficiency(%)
0.12	0.0724	60.33%	61.40%
0.11	0.0684	62.18%	
0.1	0.0621	62.10%	
0.09	0.0547	60.78%	
0.08	0.0493	61.63%	

Table 4-1 Focusing efficiency.

doi:10.6342/NTU202404691

Then, we replaced power meter with a CMOS sensor to measure light intensity distribution of metalens. Fig. 4-18 presents the Airy disk pattern of the metalens that we measured (including the central bright fringe, the first dark ring, and the second bright ring), while Fig. 4-19 displays the light intensity distribution.

From Fig. 4-18, it was observed that the effective area of the metalens is not the designed 1500 μm. However, no significant fabrication defects were identified in the SEM and OM images taken during the fabrication process. Therefore, I speculate that the issue might have occurred during the scaling and stacking of the metalens from the designed 60 μm to 1500 μm, resulting in an effective area that does not match the design. The measured effective area is approximately 562.35 μm.

doi:10.6342/NTU202404691

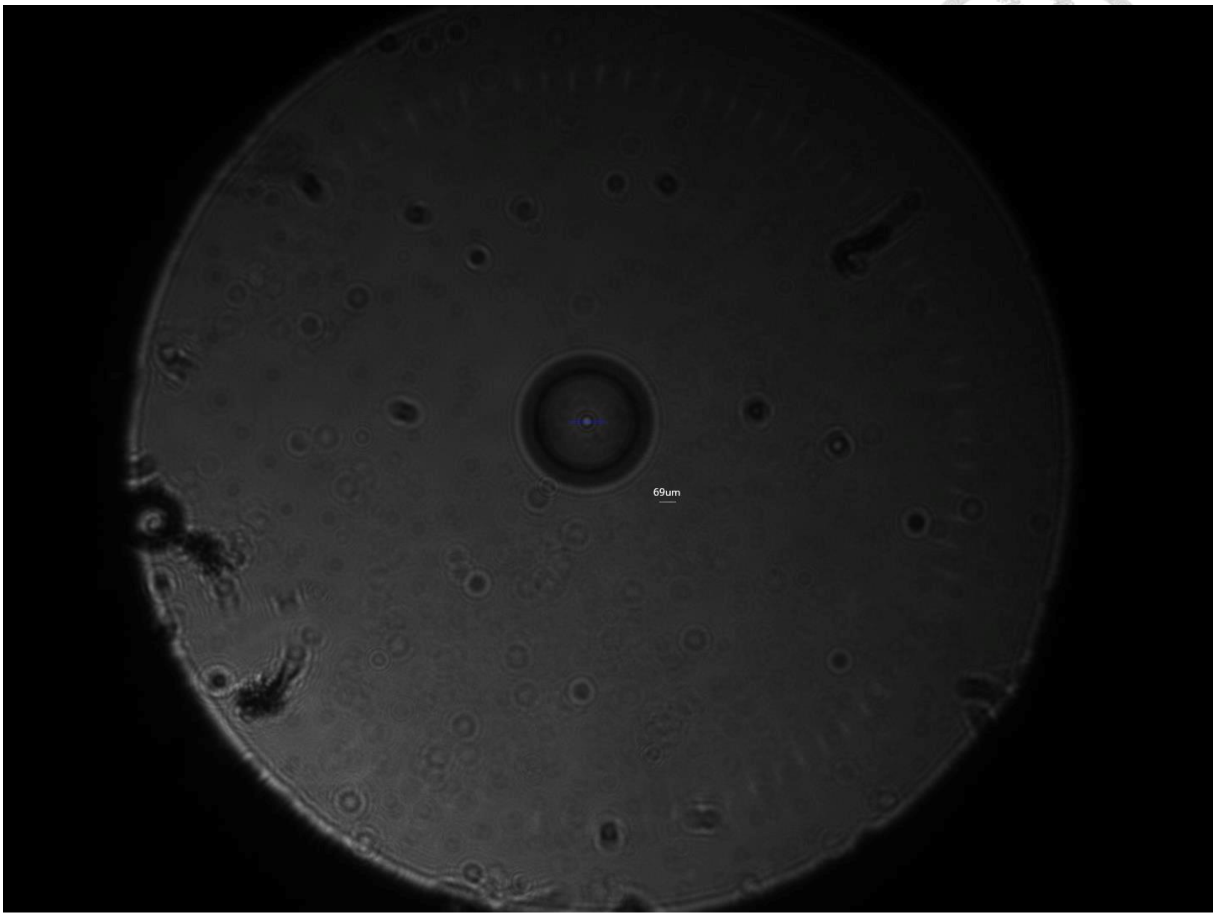

Fig. 4-18 the airy disk of measurment

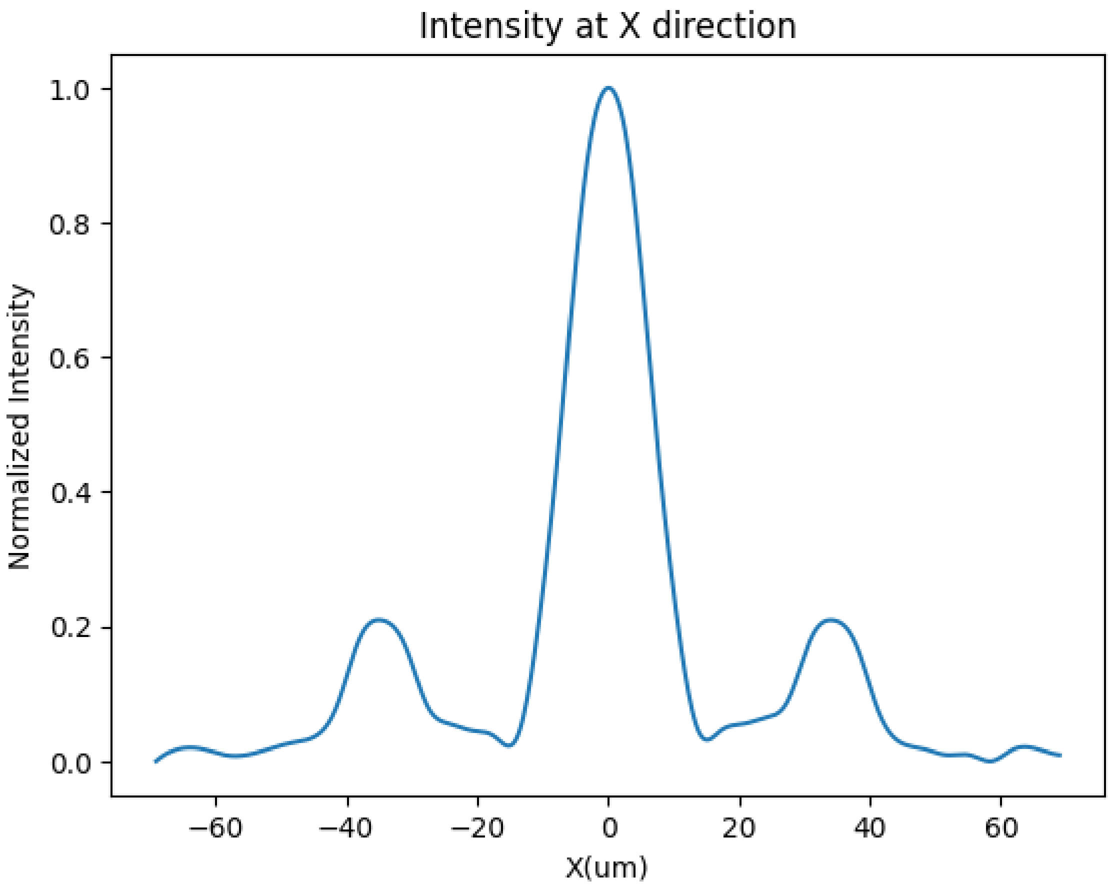

Fig. 4-19 Light intensity distribution of metalens

Measured Airy disk diameter is 31.05 μm, which means the measured Airy disk radius is 15.525 μm. According to the Rayleigh criterion, when central peak of diffraction pattern of a point source overlaps with the first dark ring of another. (i.e., distance is exactly Airy disk radius), the two point sources are considered resolvable.

From this, the minimum resolution of the metalens is determined to be 15.525 μm.

Once the quality of the metalens is confirmed, we then integrate the metalens with the CMOS to create a micro infrared camera, changing the light source to a 940 nm LED.

doi:10.6342/NTU202404691

First, we illuminate a resolution test chart with the 940 nm LED and use the camera to capture the reflected light for imaging. We position the camera along the optical axis of the reflected light at distances of 8 cm.

We used the above method to capture photos of the resolution test chart. First, we measured the width of a set of bright and dark stripes in the photo to determine the corresponding spatial frequency for that line pair, as shown in Fig. 4-20.

Fig. 4-20 the corresponding spatial frequency for the line pair.

Next, we measured the maximum brightness I_{max} and minimum brightness I_{min} for each set of stripes to calculate the contrast for that line pair. The contrast is calculated using the following formula:

$$Contrast(\%) = \frac{Imax - Imin}{Imax + Imin} \qquad (4.2.2)$$

This provided the data point for the line pair. By measuring multiple line pairs, we plotted the MTF (Modulation Transfer Function) chart to analyze the resolution of the camera.

Since the bright and dark stripes on the resolution test chart are not of equal width (1:1), and the actual size of the resolution test chart differs from the 1951 USAF resolution test chart, the measured contrast may also deviate accordingly.

MTF (Modulation Transfer Function) is a method of measuring a camera's capability to convert contrast into image quality, describing the level of contrast a lens maintains at a specific resolution, such as Y % contrast at X lp/mm. Here, (lp/mm) is a measurement unit indicating the number of alternating dark and bright line stripes (line pairs) that can be resolved within one millimeter of an image.

doi:10.6342/NTU202404691

For example, 1 lp/mm means there is a line pair (i.e., one bright line + one dark line stripes) within a 1mm distance. Similarly, 10 lp/mm means there are ten line pairs within 1mm (ten bright lines + ten dark lines stripes). Therefore, a higher lp/mm value indicates that the camera can capture finer details.

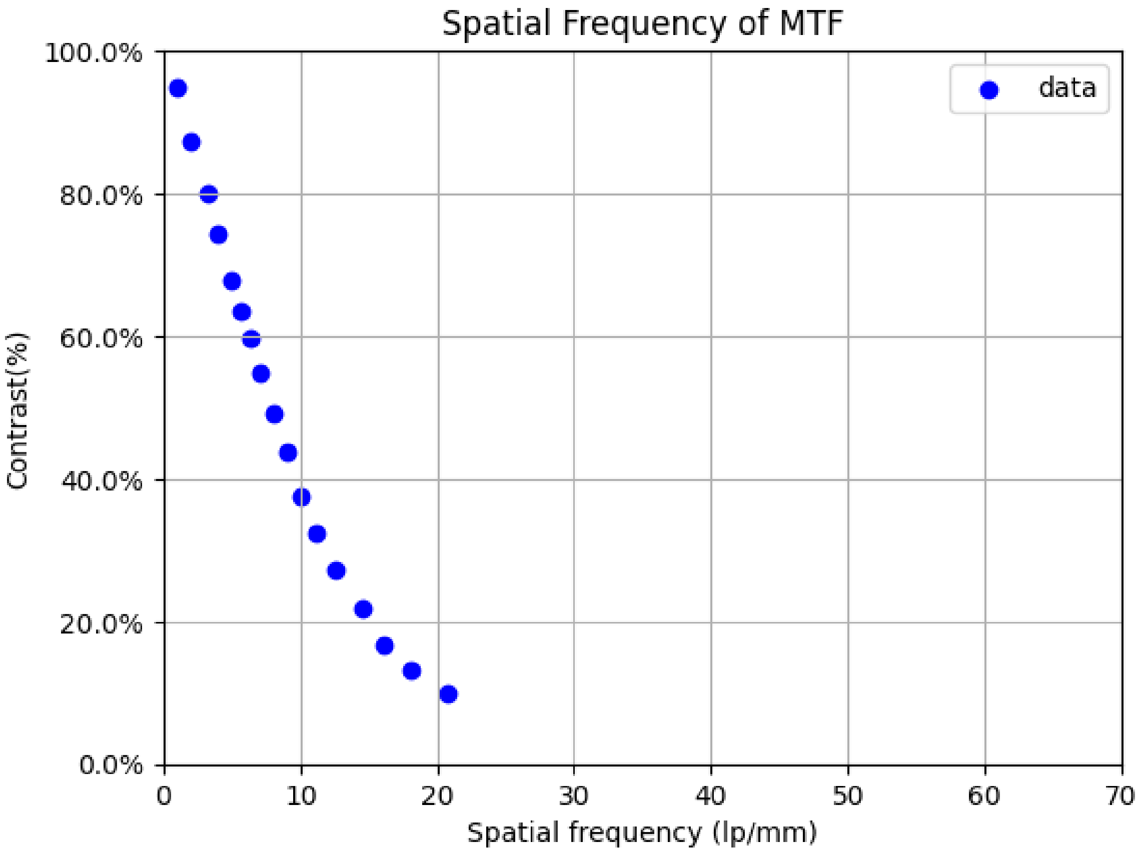

Fig. 4-21 The Frequency MTF graph.

Experimental results are depicted in Fig. 4-21, indicate that as lp/mm increases, the contrast the camera can resolve gradually decreases.

doi:10.6342/NTU202404691

Finally, we use the integrated micro-camera to perform simple pupil tracking. First, we replace the resolution test chart with a human eye as the target and direct infrared light from a 940 nm LED towards the eye. Since we use a low-power 940 nm infrared LED, it does not harm the eye. The infrared light reflected from the pupil is focused onto the CMOS sensor by the metalens, forming a picture of human eye, as display in Fig. 4-22.

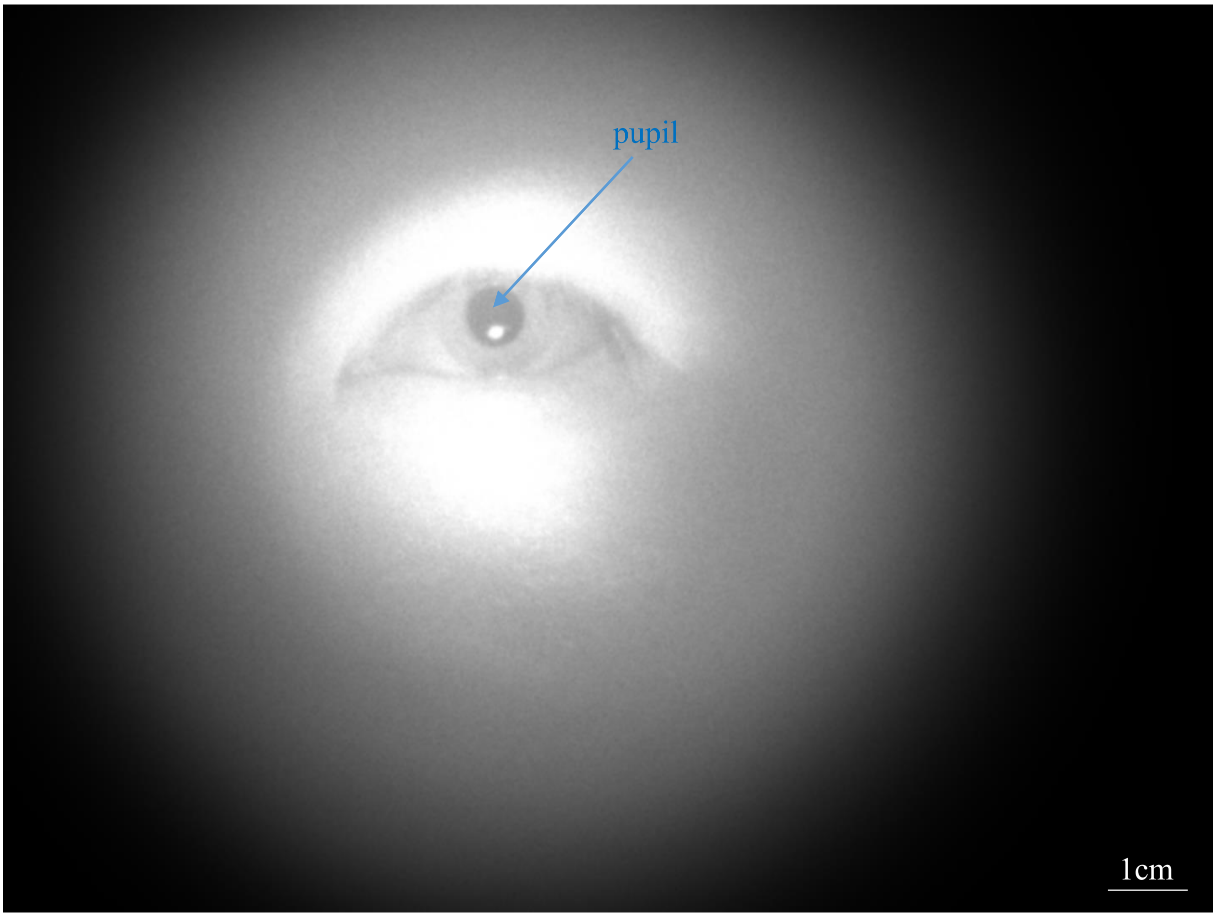

Fig. 4-22 Picture of human eye.

In Fig. 4-22, we can clearly see the structure of the human eye, particularly the pupil.

doi:10.6342/NTU202404691

Despite this, the photos we captured are sufficient for the computer to detect the pupil's position. We used open-source pupil detection software available on a public platform [26] to recognize precise location of pupil in photo. Pupil was outlined and marked for positioning, with its center and actual size also indicated. The final results are presented in Fig. 4-23. This indicates that the micro-camera has the capability for pupil detection.

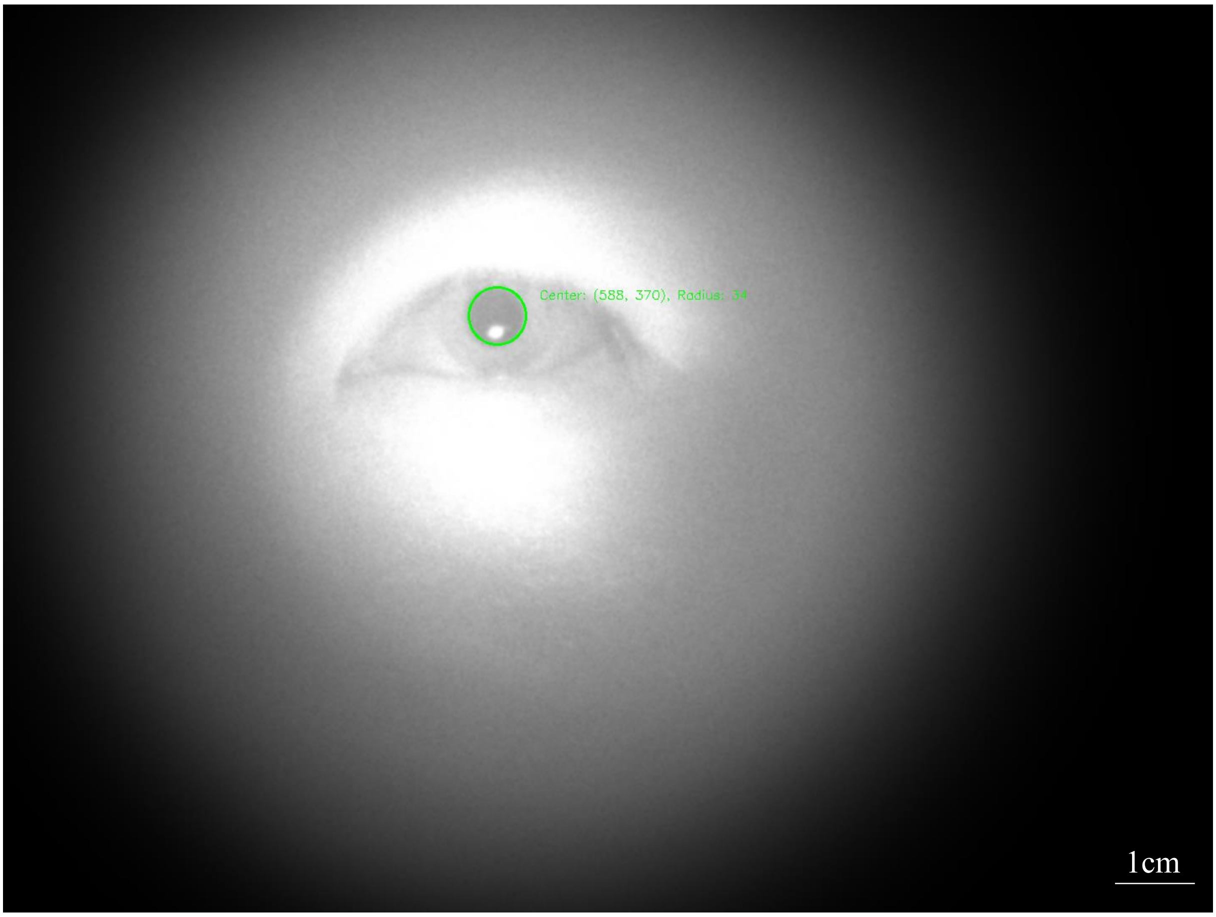

Fig. 4-23 The picture of pupil detection

4.3 Future Application

With advancements in technology, the quality requirements for lenses are gradually increasing. While traditional lenses have many advantages, such as being cost-effective and easy to produce compared to metalenses, their sizes typically range from millimeters to centimeters, making them relatively bulky. Furthermore, as consumer demands become more diverse, it often requires the use of lens combinations to meet users' needs. For example, a lens that can simultaneously focus, correct chromatic aberration, and capture wide-angle images would need to combine focusing lenses, achromatic lenses, and wide-angle lenses, resulting in traditional lenses being cumbersome.

On the other hand, while metalenses are more expensive and harder to produce, their sizes typically range from micrometers to millimeters, significantly reducing the volume of the lenses. As semiconductor manufacturing technologies mature, the costs are expected to decrease gradually, and production quantities will increase year by year. The aforementioned demands can be addressed through design by creating corresponding patterns, allowing metalenses to have the advantage of being compact and lightweight. In the future, they hold great potential in the fields of medical applications and AR/VR.

For example, in pupil detection, the size and bulkiness required by traditional lenses are much greater than those of metalenses, as shown in Figures 4-24 and 4-25.

doi:10.6342/NTU202404691

Fig. 4-24 The traditional lens

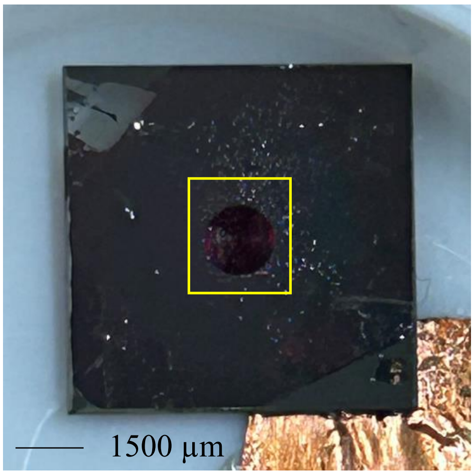

Fig. 4-25 The metalens

doi:10.6342/NTU202404691

Chapter 5 Summary

In this thesis, we chose amorphous silicon (a-Si) as the material for the metalens. We applied a 570 nm thick layer of a-Si onto a glass substrate. Subsequently, we performed a lithography process by spin-coating HMDS and positive photoresist onto the sample surface, using electron beam lithography to expose the pattern on the sample surface, followed by development to retain the pattern on the photoresist. Then, we deposited a 50 nm-thick layer of metal (nickel) as a blocking layer with electron beam evaporation. Subsequently, a lift-off step was performed to transfer the image from the photoresist to the metal. The sample was then placed in an ICP-RIE system for dry etching, with O_2 and SF_6 introduced to etch the a-Si. Following this, the sample was immersed in a solution of H_2SO_4 and H_2O_2 in a 2:1 ratio for wet etching to remove the nickel blocking layer above the nanopillars. Through these fabrication steps, we obtained a metalens with a diameter of 1500 μm that features a-Si nanopillars.

Subsequently, we measured the focusing efficiency using various optical measurement methods. The focusing efficiency achieve 61.4%. Based on the measurement results of the Airy disk, the minimum resolution is 15.525 μm. Next, we paired the fabricated metalens with a CMOS sensor to assemble a micro infrared camera,

doi:10.6342/NTU202404691

capturing images of the resolution target and plotting the MTF curve for this camera. Finally, we successfully performed pupil detection using this micro camera.

Through the aforementioned semiconductor fabrication techniques and optical measurements, we confirmed that this camera can perform pupil detection, achieving preliminary success. In the future, there is potential to integrate this micro camera with medical devices or AR/VR glasses to realize the miniaturization of object detectors and enhance the application of metalenses in various fields.

doi:10.6342/NTU202404691

REFERENCE

[1] A. Arbabi and A. Faraon, "Advances in optical metalenses," *Nat. Photonics,* Review vol. 17, no. 1, pp. 16-25, Jan 2023, doi: 10.1038/s41566-022-01108-6.

[2] I. Moreno, "Optics of the metalens," *Eur. J. Phys.,* Article vol. 43, no. 6, p. 11, Nov 2022, Art no. 065302, doi: 10.1088/1361-6404/ac93c8.

[3] N. Yu and F. Capasso, "Flat optics with designer metasurfaces," *Nature Materials*, vol. 13, no. 2, pp. 139-150, 2014, doi: 10.1038/nmat3839.

[4] C. E. Gutierrez and A. Sabra, "Chromatic aberration in metalenses," *Adv. Appl. Math.,* Article vol. 124, p. 26, Mar 2021, Art no. 102134, doi: 10.1016/j.aam.2020.102134.

[5] Z.-B. Fan *et al.*, "A broadband achromatic metalens array for integral imaging in the visible," *Light: Science & Applications,* vol. 8, no. 1, p. 67, 2019, doi: 10.1038/s41377-019-0178-2.

[6] W. T. Chen *et al.*, "A broadband achromatic metalens for focusing and imaging in the visible," *Nature nanotechnology,* vol. 13, no. 3, pp. 220-226, 2018, doi: 10.1038/s41565-017-0034-6.

[7] M. Khorasaninejad *et al.*, "Achromatic Metalens over 60 nm Bandwidth in the Visible and Metalens with Reverse Chromatic Dispersion," *Nano Lett.,* Article vol. 17, no. 3, pp. 1819-1824, Mar 2017, doi: 10.1021/acs.nanolett.6b05137.

[8] M. Khorasaninejad *et al.*, "Polarization-insensitive metalenses at visible wavelengths," *Nano Lett.,* vol. 16, no. 11, pp. 7229-7234, 2016, doi: 10.1021/acs.nanolett.6b03626.

[9] M. Khorasaninejad, W. T. Chen, R. C. Devlin, et al., “Metalenses at visible wavelengths: Diffraction-limited focusing and subwavelength resolution imaging,” Science 352(6290), 1190–1194, 2016, doi: 10.1126/science.aaf6644.

[10] Z. Liu, D. Wang, H. Gao, et al., “Metasurface-enabled augmented reality display: a review,” Adv. Photonics 5(03), 034001, 2023, doi: 10.1117/1.AP.5.3.034001.

doi:10.6342/NTU202404691

[11] A. Arbabi, E. Arbabi, Y. Horie, et al., “Planar metasurface retroreflector,” Nat. Photonics 11(7), 415–420, 2017, doi: 10.1038/nphoton.2017.96.

[12] R. Fu, Z. Li, G. Zheng, et al., “Reconfigurable step-zoom metalens without optical and mechanical compensations,” Opt. Express 27(9), 12221–12230, 2019, doi: 10.1364/OE.27.012221.

[13] C. Gennarelli, A. Capozzoli, L. J. Foged, et al., “Recent advances in near-field to far-field transformation techniques,” International Journal of Antennas and Propagation, 2012, doi: 10.1155/2012/243203.

[14] A. Arbabi, Y. Horie, A. J. Ball, et al., “Subwavelength-thick lenses with high numerical apertures and large efficiency based on high-contrast transmitarrays,” Nat. Commun. 6(1), 7069, 2015, doi: 10.1038/ncomms8069.

[15] Xin Jin *et al.*, "Eye-Tracking in AR/VR: A Technological Review and Future Directions," *IEEE Open Journal on Immersive Displays,* vol. 1, pp.146-154, 2024, doi: 10.1109/OJID.2024.3450657.

[16] C. S. Lin *et al.*, "Polar Coordinate Mapping Method for An Improved Infrared Eye-Tracking System," *Biomedical Engineering: Applications, Basis and Communications*, vol. 17, no. 03, pp. 141-146, 2005, doi: 10.4015/S1016237205000226.

[17] H. Kitabayashi, *et al.*, "Development of High Power Infrared LED," *SEI Technical review,* vol. 70, no.71, 2010.

[18] C.H. Morimoto *et al.*, "Pupil detection and tracking using multiple light sources," *ScienceDirect*, vol. 18, no.4, pp. 331-335, Mar 2000, doi: 10.1016/S0262-8856(99)00053-0.

[19] C. Y. Fan, T. J. Chuang, K. H. Wu, and G. D. J. Su, "Electrically modulated varifocal metalens combined with twisted nematic liquid crystals," *Opt. Express,* Article vol. 28, no. 7, pp. 10609-10617, Mar 2020, doi: 10.1364/oe.386563.

[20] M. Altissimo, "E-beam lithography for micro-/nanofabrication," *Biomicrofluidics,* vol. 4, no. 2, p. 026503, 2010, doi: 10.1063/1.3437589.

[21] C. Vieu *et al.*, "Electron beam lithography: resolution limits and applications," *Applied surface science,* vol. 164, no. 1-4, pp. 111-117, 2000, doi: 10.1016/S0169-4332(00)00352-4.

[22] J. Vac., "UV/ozone cleaning of surfaces," *Vacuum Science & Technology A,* vol. 3, no. 3, pp. 1027–1034, 1985.

[23] G. M. Wu et al., "InGaN/GaN multiple quantum wells with surface micro hole array structures," *IEEE NANO*, vol.7, pp.498-501, 2007, doi: 10.1109/NANO.2007.4601240.

[24] A.-S. Rollier et al., "High yield grafting of carbon nanotube on ultra-sharp silicon nanotips: Mechanical characterization and AFM imaging," *IEEE MEMS*, vol.20, p.878, 2007, doi: 10.1109/MEMSYS.2007.4433179.

[25] G. E. Mustoe, "Uranium Mineralization of Fossil Wood," *Geosciences*, vol.10, no.4, p.133., 2020, doi: 10.3390/geosciences10040133.

[26] S. Esmitt, "Gist: Pupil detection sample," GitHub. [Online]. Available: https://gist.github.com/esmitt/61edc8ed6ccbc7a7e857074299449990.

doi:10.6342/NTU202404691